

Enhancing Sensitivities to Long-lived Particles with High Granularity Calorimeters at the LHC

Jia Liu,¹ Zhen Liu,² Lian-Tao Wang,^{1,3} and Xiao-Ping Wang⁴

¹*Enrico Fermi Institute, University of Chicago, Chicago, IL 60637, USA*

²*Maryland Center for Fundamental Physics, Department of Physics,
University of Maryland, College Park, MD 20742, USA*

³*Department of Physics, University of Chicago, Chicago, IL 60637, USA*

⁴*High Energy Physics Division, Argonne National Laboratory, Argonne, IL 60439, USA*

(Dated: March 18, 2022)

The search for long-lived particles (LLP) is an exciting physics opportunity in the upcoming runs of the Large Hadron Collider. In this paper, we focus on a new search strategy of using the High Granularity Calorimeter (HGCal), part of the upgrade of the CMS detector, in such searches. In particular, we demonstrate that the high granularity of the calorimeter with this upgrade, which allows us to see “shower tracks” in the calorimeter, can play a crucial role in identifying the signal and suppressing the background. We study the potential reach of the HGCal using a signal model in which the Standard Model Higgs boson decays into a pair of LLPs, $h \rightarrow XX$. After carefully estimating the Standard Model QCD and the misreconstructed fake-track backgrounds, we give the projected reach for both a more conservative vector boson fusion trigger and a novel displaced-track-based trigger. Our results show that the best reach for the Higgs decay branching ratio, $\text{BR}(h \rightarrow XX)$, in the vector boson fusion channel is about $\mathcal{O}(10^{-4})$ with lifetime $c\tau_X \sim 0.1\text{--}1$ meters, while for the gluon gluon fusion channel it is about $\mathcal{O}(10^{-5}\text{--}10^{-6})$ for similar lifetimes. Alternatively, for an LLP with $c\tau_X \sim 10^3$ meters, the HGCal based search should be able to probe $\text{BR}(h \rightarrow XX)$ down to a few $\times 10^{-4}(10^{-2})$ in the gluon gluon fusion (vector boson fusion) channels, respectively. In comparison with these previous searches, our new search shows enhanced sensitivity in complementary regions of the LLP parameter space.

Contents

I. Introduction	2
II. Analysis framework	5
A. Signal model: long-lived particles from Higgs decay	5
B. Modeling the HGICAL detector	6
C. Signal and Background generation	7
The long-lived particle signal	7
SM QCD background	8
Fake-track background	8
D. Triggering strategy	9
III. The kinematics of signal and backgrounds	10
A. The Displaced Vertex fitting variables	11
B. The transverse impact parameter distribution	18
C. Correlations between the selection cuts	18
IV. The Results	23
A. Cut efficiencies	23
B. The reach	26
V. Conclusion	27
VI. Appendix	28
References	36

I. Introduction

Models of new physics beyond the Standard Model (BSM) often predict the existence of long-lived particles (LLPs), giving rise to distinct signatures at colliders (see [1] for a recent review). There have been many searches for LLPs at the ATLAS, CMS, and

LHCb experiments at the Large Hadron Collider (LHC). The signatures of the LLP depend on its charge, lifetime, and decay products. Accordingly, various search strategies and detection techniques can be used, including the non-prompt photon detection using the electromagnetic (EM) calorimeter [2, 3], the disappearing track search based on the tracking system [4–6], and the displaced leptons or lepton jets search based on the tracking system [7–13], the calorimeter [14, 15], as well as the muon system [16–18]. Many new search targets and strategies for the LLPs based on the LHC experiment have also been proposed [19–65].

In this work, we focus on a new sub-detector HGICAL, a highly granular and silicon-based calorimeter, which is the Phase-2 upgrade of the CMS endcap calorimeter [66]. It consists of a sampling calorimeter with silicon and scintillators as active material, including both the electromagnetic and the hadronic sections with unprecedented fine segmentation. In particular, each section consists of silicon cells of size ($0.5 - 1 \text{ cm}^2$) and the remainder of the hadron calorimeter will use highly-segmented plastic scintillators of size ($4 - 30 \text{ cm}^2$) [66]. It has an intrinsic high-precision timing capability from silicon sensors with a resolution of $\sim 25 \text{ ps}$. Due to its fine transverse granularity, the HGICAL has an angular resolution of about 5×10^{-3} radians for electromagnetic shower with $p_T > 20 \text{ GeV}$, after taking into account the broadening effect from the shower. The HGICAL can handle different LLPs signatures. It also serves as a semi-forward detector different from most LLP studies at LHC main detectors that are mainly based on central detectors.

We carefully simulated and estimated the SM background for generic LLP signals, which contains prompt and displaced QCD background and non-prompt misconnected fake-track background. Based on these, we design a set of cuts that take advantage of the unique features of the signal and the capabilities of the HGICAL detector. We use a signal model in which scalar LLPs (X) are produced from SM Higgs decay ($h \rightarrow XX$). This simple model is quite representative [68], covering a broad range of new physics scenarios, such as the hidden valley models [69–71], and more recent proposals motivated by neutral naturalness [72–77]. Two production channels of SM Higgs are considered. One is the vector boson fusion (VBF) channel, together with the existing VBF trigger. The other is the gluon-gluon fusion (ggF) channel with a potential displaced track trigger, enabled by new trigger considerations from the tracker and HGICAL. The sensitivity of HL-LHC is given as a function of the proper lifetime of X , shown in Fig. 1. The best reach for VBF channel is about $\text{BR}(h \rightarrow XX) \sim \mathcal{O}(10^{-4})$ with a lifetime of $c\tau_X \sim 0.1\text{--}1$ meters, while for the ggF channel it is

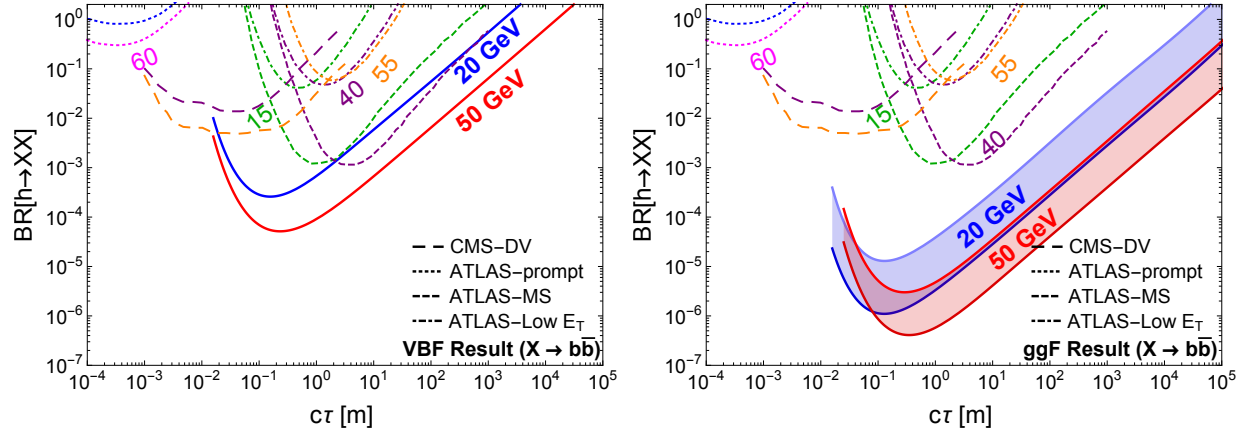


FIG. 1. The projected sensitivity for Higgs decays to long-lived particles with VBF trigger (left panel) and a displaced track trigger for the ggF channel (right panel) at the HL-LHC as a function of proper lifetime of X using our proposed HGCAL LLP search. We consider two scenarios of the displaced track trigger. The solid line on the top of the shaded region corresponds to the reach with a trigger requirement of $H_T > 100$ GeV, while the solid line on the bottom of the shaded region is obtained without such a requirement. The existing limits for $\text{BR}(h \rightarrow XX)$ from ATLAS Run 2 searches based on prompt VH [67] (dotted), the muon spectrometer [18] (dashed), the calorimeter [14] (dot-dashed), and the CMS search based on displaced vertex in the tracker system [13] (long dashed), are also shown for comparison. The numbers on different colored lines indicate the mass of the LLP in units of GeV for the corresponding searches.

about $\text{BR}(h \rightarrow XX) \sim \mathcal{O}(10^{-5}-10^{-6})$ for similar lifetime. Alternatively, for an LLP with $c\tau_X \sim 10^3$ meters, the HGCAL based search should be able to probe $\text{BR}(h \rightarrow XX)$ down to a few $\times 10^{-4}$ (10^{-2}) in the ggF (VBF) channels, respectively.

The paper is organized as follows. In Sec. II A, we discuss the signal model and the trigger considerations for the signal. In Sec. II C, we describe signal and background generation. In Sec. III, the distributions of kinematic variables are discussed, and the corresponding cuts are applied. Finally, we show our results in Sec. IV and conclude in Sec. V.

II. Analysis framework

A. Signal model: long-lived particles from Higgs decay

To demonstrate the potential of our proposed search, we use a signal model in which the LLP couples to the SM through the Higgs portal. For $m_X < m_h/2$, the LLP will be produced through the Higgs boson decay

$$h \rightarrow XX. \quad (1)$$

We assume X is a neutral and meta-stable scalar which will further decay via $X \rightarrow \bar{b}b$. The free parameters in this simplified model are mass m_X , lifetime $c\tau_X$, and the decay branching ratio $\text{BR}(h \rightarrow XX)$.

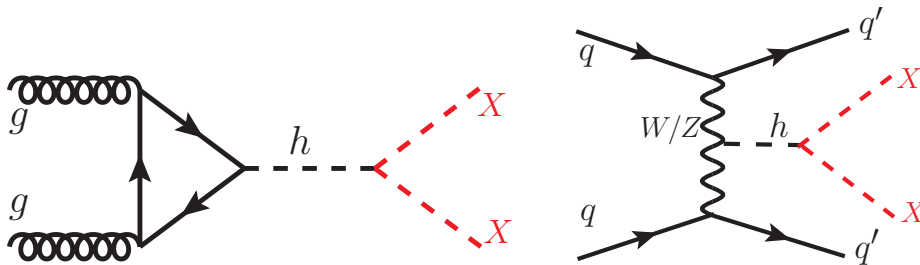


FIG. 2. The processes of producing the long-lived particle X from SM Higgs decay considered in this study. Left panel: gluon-gluon fusion Higgs production. Right panel: vector boson fusion Higgs production.

We consider two Higgs production channels, namely, the VBF production and ggF production, shown in Fig. 2. The VBF channel is motivated by the possibility of using an existing VBF trigger that does not rely on the properties of the LLP. In the ggF channel, we will explore the physics potential of using displaced track triggers after LHC Phase-2 upgrades, e.g., Ref. [78]. Since the metastable particle X is neutral, it does not leave a track as it traveling through the detector. Subsequently, X decays to $\bar{b}b$. For our work, we do not use the information of whether the jets are initiated by heavy or light flavor quarks.¹

¹ In principle, the secondary displacement from the heavy-light mesons, such as B mesons and Kaons can help to identify the specific property of the LLPs.

B. Modeling the HGICAL detector

Our study focuses on the potential of the LLP search of the HGICAL detector [66]. Due to the novelty of the detector and the signature, we cannot perform a full-fledged detector simulation. Instead, we make assumptions based upon the HGICAL performance document. We describe here the relevant detector parameters used in our study.

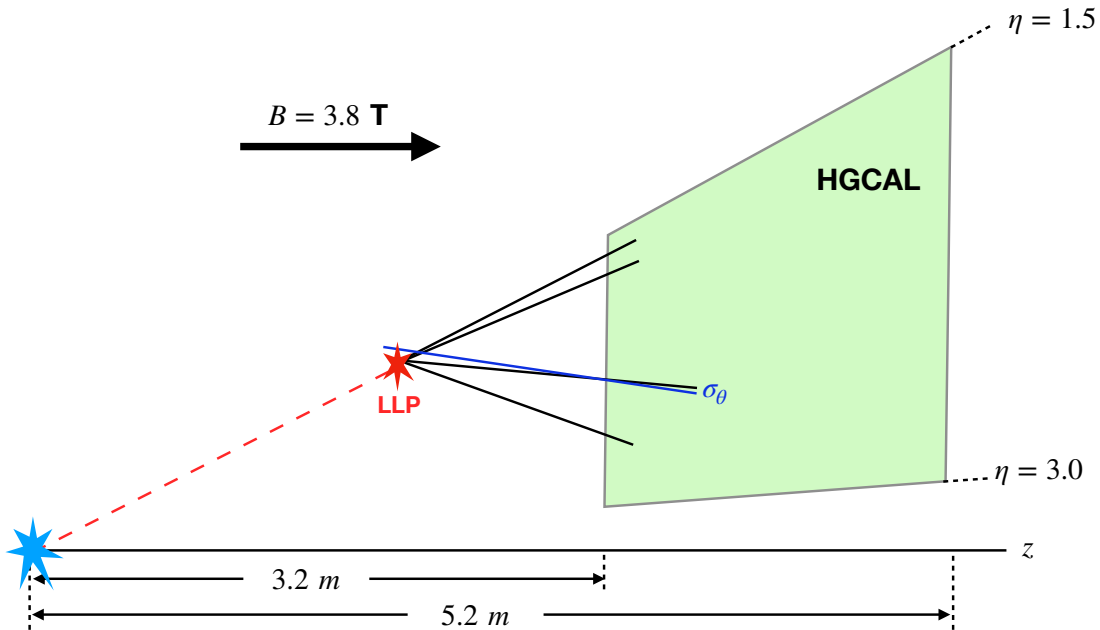


FIG. 3. A schematic drawing for the decay products of the long-lived particle arriving the HGICAL. The direction of the momentum of the decay products can be measured by the HGICAL with an angular resolution of σ_θ , resulting in an error in reconstructing the displaced vertex.

The HGICAL detector locates at $|z| = 3.2$ m and extends to $|z| = 5.2$ m. The angular coverage of the detector is $1.5 < |\eta| < 3.0$. Its stand-alone angular resolution on the shower direction is taken to be $\sigma_\theta \sim 5 \times 10^{-3}$ radians, with possible improvement when combining with the information from the inner detectors.² A schematic plot for the long-lived particle signal arriving the HGICAL is shown in Fig. 3. The particle will travel in a magnetic field of $B = 3.8$ Tesla along the z direction, therefore, it would follow a helical trajectory. We require the tracks to go through the first layer of HGICAL at $|z| = 3.2$ m. The tracks with

² We note here in the text we will not distinguish tracks and shower when discussing HGICAL, since the shower can be viewed as a “fat track”. A subtle difference is HGICAL will be able to see neutral particles shower as well, which traditionally do not correspond to tracks.

p_T above 1 GeV can be reconstructed at L1 level [66]. Each point on the track trajectory has a 4D coordinate, (t, x, y, z) . Once the momentum of a particle at a point on the track is known, the 4D trajectory of the full track can be calculated.

The directions of particles reaching HGICAL can be measured with an angular resolution of σ_θ . The inaccuracy in measuring its direction is a main source of the error in the measurement of the track direction, which can fake our signal. We smear the direction of the momentum using a Gaussian function with a spread equal to the angular resolution σ_θ . With this new momentum for the particle at the first layer of HGICAL, we then recalculate its 4D spiral trajectory.

C. Signal and Background generation

The long-lived particle signal

The signal events at parton level are generated using `MadGraph5_aMC@NLO` [79], and the parton shower is performed by `Pythia8` [80, 81]. The charged particles with $p_T > 1$ GeV are kept as track candidates.

For the signal, the displaced tracks dominantly come from the displaced decay of the LLP X , which will give a displaced vertex (DV). The location and time of this DV results from a convolution of X momentum distribution and the lifetime of X . We also require X to decay within $|z| < 1.5$ m to ensure the tracks have five stubs in the tracker. Given the 4D vertex information and the 4-momentum of each charged particle at that vertex, one can reconstruct its 4D helical trajectory in the magnetic field. From this, we obtain the 3-momentum of the particle when it arrives at the HGICAL. We then smear the direction of its momentum and recalculate the 4D trajectory.

A further improvement of the HGICAL coverage can be achieved by considering LLPs decaying inside HGICAL. The LLP signal would appear as showers with an anomalous shape in the HGICAL. However, given the difficulty of modeling the showering pattern in this material-dense area and the lack of understanding of the background, we take the rather *conservative* class of signals in which X decay before entering HGICAL. In this case, we use HGICAL to *only* pick out the displaced tracks. These tracks are identified via the showering of the hadronic particles from the LLP decay. Hence, they have a degraded

angular resolution than the HGICAL physical limitations due to the broadening caused by interaction with materials.³ We also require these tracks to match hits in the outer part of the tracking system, which picks only the charged components of the signal. This is clearly a very conservative use of the HGICAL capability and leaves a large room for future improvement with a full understanding of the HGICAL performance.

SM QCD background

The main SM prompt backgrounds are the QCD dijet events, including bottom quark pair $b\bar{b}$. A main feature of the signals is the presence of tracks with large transverse impact parameters. There are two reasons for such a QCD background to also have displaced tracks. The first one is the finite lifetime of mesons and baryons. The second one is from the finite angular resolution of HGICAL.

We use MadGraph5_aMC@NLO [79] and Pythia8 [80, 81] to generate the SM background events, which properly include the finite lifetime effect of SM mesons and baryons. The displaced tracks come primarily from K_S^0 meson ($c\tau \sim 2.7$ cm), with some addition contribution from heavy baryons like Λ^0 ($c\tau \sim 7.8$ cm).

After applying generator level cuts such as $p_T > 20$ GeV at the parton level, the cross-sections of $b\bar{b}$ and jj are 3.6×10^6 pb and 1.7×10^8 pb⁴, respectively. The jet matching has been applied with one extra jet added and the minimal k_t is set to be 30 GeV. After hadronization, charged tracks with $p_T > 1$ GeV are kept. Among the tracks arriving at HGICAL, we kept the five leading ones to be smeared⁵.

Fake-track background

We denote as fake-track background the events with mis-reconstructed tracks from the accidental connections of the hits in the tracker system. They can easily have very large d_0 , similar to those from the signal. There are $\mathcal{O}(30)$ such tracks per bunch crossing. This high combinatorics makes it possible for a selection of a few tracks to approximately form a

³ We take this into account by using a degraded angular resolution.

⁴ Here we use the 4-flavor PDF scheme.

⁵ This procedure tends to overestimate the suppression provided by our vertexing cuts. However, since our results essentially do not rely on the vertexing cuts for suppressing the SM QCD background, we keep only the five leading tracks for simplicity.

vertex.

We follow Ref. [82, 83] to generate events with mis-reconstructed tracks. We also add the timing information to the tracks, which can potentially further reduce the background [84]. To generate a fake-track, we use a set of kinematical variables following a flat distribution within the ranges indicated below.

- $\phi_0 \in [0, 2\pi]$: the azimuthal angle of a reference point from the beam spot in the x - y plane.
- $z_0 \in [-0.15, 0.15]$ m: the z coordinate of the reference point.
- $t_0 \in [-6, 6]$ nanosecond: the time coordinate of the reference point.
- $d_0 \in [10^{-3}, 0.15]$ m: the transverse impact parameter of the track.
- $q/R \in [0, (1.75 \text{ m})^{-1}]$: the inverse of the track curvature in x - y plane.
- $\eta \in [-3, 3]$: the pseudo-rapidity of the direction of the track at the reference point.

The reference point is defined at the location of the transverse impact parameter of a given track. The curvature of the track and the transverse momentum of the presumed particle responsible for it satisfy $R = |p_T/(q \times B)| = (p_T/\text{GeV}) \times 0.88 \text{ m}$. q is the charge of the particle, assumed to be $\pm e$ with equal probability. From the range of the curvature, the tracks generated must have $p_T \geq 2 \text{ GeV}$, with a flat probability in p_T^{-1} . In the x - y plane, the trajectory of the track is a circle with a radius equals to R . However, the origin (the beam spot) can be either inside or outside the circle. The distance between the center of the circle and the origin can be either $R - d_0$ or $R + d_0$. We assume the two cases occur with equal probability. With these parameters, the 4D trajectory of the fake tracks can be determined.

D. Triggering strategy

For the VBF channel, we require at least one forward jet $p_T > 110 \text{ GeV}$, and both of the forward jets $p_T > 35 \text{ GeV}$ with an invariant mass $m_{jj} > 620 \text{ GeV}$ [85].

For the ggF channel, we try two different trigger strategies. First, we use a proposed L1 displaced track trigger cuts with $H_T > 100 \text{ GeV}$, which has been demonstrated with two

displaced tracks with $p_T > 2$ GeV within an L1 jet [78]. This L1 trigger rate is about 10 kHz in the central region and about a factor of 2–3 higher in the endcap region [78]. We require our signals to have more than five displaced tracks and $H_T > 100$ GeV, which is more stringent than Ref. [78]. Nevertheless, we still assume the same level of L1 trigger rate of 10 kHz. Because that displaced track selection and vertex reconstruction do provide suppression of the L1 rate, the average number of multiple track bundles passing all these trigger requirements should be around one per triggered event. Given that the HL-LHC will run for 10^8 seconds, the total number of such fake-track bundle events is about 1×10^{12} .

The second trigger strategy for the ggF channel is a displace track trigger without the H_T cut. It makes use of five displaced tracks with a vertex fitting, rather than the two displaced tracks [78]. This should reduce the low-level trigger rate and allow for the removal of the H_T requirement. We also emphasize that these randomly connected tracks may not be corresponding calorimeter energy deposits in the HGCal. Even if our estimate of the tracking alone suppression is not sufficient, consistency matching between different sub-detectors of the experiment will provide sufficient suppression.

III. The kinematics of signal and backgrounds

There are two main characteristics of the signal. First, the signal tracks tend to have large impact parameter, d_0 . Hence, requiring a number of tracks (five in our case) to have large d_0 allows us to effectively separate the signal from the QCD background, which is mostly prompt. On the other hand, the fake-track background have a flat distribution in a large range of d_0 . This is where the second main characteristic comes into play. Namely, the signal tracks all originate from a single vertex. Since each fake-track is independent of each other, they have a small probability of reconstructing a common vertex. In the following, we will define a set of variables to quantify this feature. We note that if the tracks are generated via interaction with detector material, there would be a reconstructable displaced vertex. One could veto all the displaced vertices in the material-dense region, as has been done by many LLP searches [1, 8, 86].

A. The Displaced Vertex fitting variables

We fit the candidate tracks to a displaced vertex and define associated fitting variables as follows. We begin with five leading (in p_T) tracks and calculate their 4D trajectories. We perform a 2D vertex fit in the transverse plane by minimizing the following quantity,

$$\Delta D \equiv \sqrt{\sum_{i=1}^5 \left(\sqrt{(x - x_i^{\text{cen}})^2 + (y - y_i^{\text{cen}})^2} - R_i \right)^2}, \quad (2)$$

where $\{x_i^{\text{cen}}, y_i^{\text{cen}}\}$ are the x - y coordinates of the center of the circle for the i th track and R_i is the transverse radius of the track helix. The minimization gives the best-fit coordinates, x and y , for a presumed DV. Of course, this fit won't be perfect in reality and the tracks will miss the DV by some amount. To quantify this, we begin by identifying a point, with coordinate (t_i, x_i, y_i, z_i) , as the one corresponding to the DV on the i th track. Since we have the full 4D trajectory of the track, we only need one parameter to identify this point. To this end, we choose to use the azimuth angle ϕ of the direction of the DV, with respect to the center of the circle of the i th track. Of course, in the ideal case in which all tracks originating from a DV are perfectly reconstructed, all of the x_i and y_i will coincide with x and y . We can define the following variables associated with a fitted DV.

- The displacement of the vertex in the transverse plane $r_{\text{DV}} \equiv \sqrt{x^2 + y^2}$ that minimizes ΔD in Eq. 2.
- The imperfectness or the uncertainty of vertex fitting, ΔD_{min} , based on the best-fit 2D vertex coordinates x and y that minimizes ΔD in Eq. 2.
- Based on the set of $\{z_i, t_i\}$ for each track that form a DV, we can define the mean value \bar{z} and \bar{t} , and their standard deviations σ_z and σ_t .
- For the i th track, we define the time delay as $\Delta t_i \equiv t_i - \sqrt{x_i^2 + y_i^2 + z_i^2}/c$. We define the time delay of the displaced vertex ($\overline{\Delta t}$) as the average of the Δt_i of the five leading tracks (in p_T) and the standard deviation $\sigma_{\Delta t}$. For a slow moving LLP which decays at the DV, Δt would be its time delay in comparison to the prompt particles propagating from the interaction point to the DV.

In summary, we can define the following kinematic variables using the above 2D-4D displaced vertex fitting procedure,

$$r_{\text{DV}}, \Delta D_{\text{min}}, \bar{t}, \bar{z}, \overline{\Delta t}, \sigma_t, \sigma_z, \sigma_{\Delta t}. \quad (3)$$

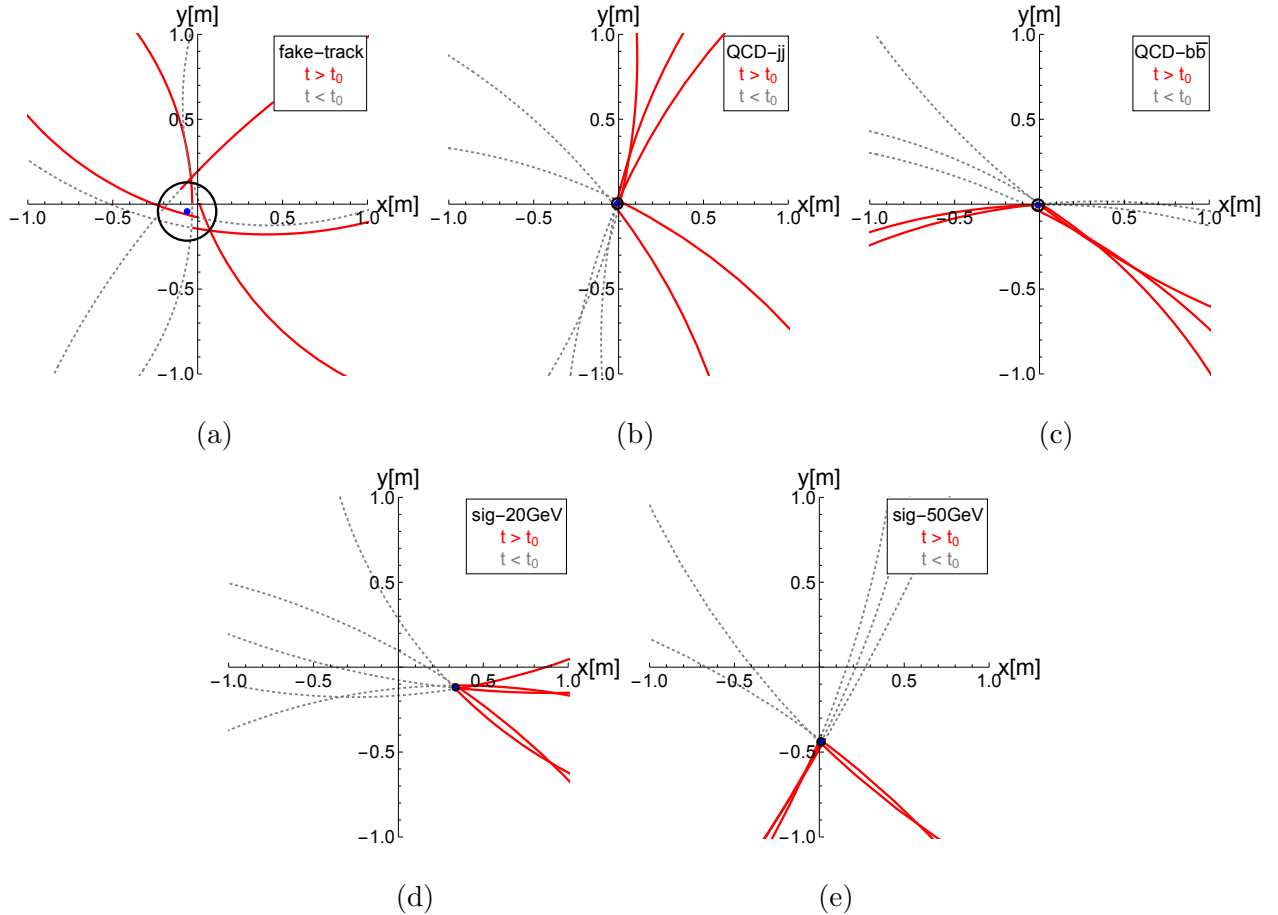


FIG. 4. Illustrative event displays in the x - y plane for the fitting algorithm with leading five displaced tracks. The blue dot is the fitted DV. The solid red (dashed gray) lines are the charged track trajectories in the event, after (before) the fitted DV. From left to right, the plots are for (a) fake-track background, (b) SM QCD light jet background, (c) SM QCD heavy-flavor jet background, (d) LLP signal with $m_X = 20$ GeV and (e) LLP signal with $m_X = 50$ GeV.

In Fig. 4, we illustrate the fitted DV location in the x - y plane and the five leading tracks in an event from the fake-track background, the QCD background, and the LLP signal. For the backgrounds, shown in (a), (b), and (c), we use solid red (dashed gray) lines for the trajectories after (before) the fitted DV. For the signal, shown in (d) and (e), we use solid red (dashed gray) lines for their trajectories after (before, extrapolated) the

LLP decay. The fitted DV location is represented by a blue dot. The black circles have a radius representing the fitted vertex uncertainty, ΔD_{\min} . A smaller black circle indicates the vertex fitting algorithm successfully identifies the location of the displaced vertex. This figure shows the different behavior of the various types of background and the signal. For the SM QCD background, the vertices have small displacement, and the fitted vertex has sizable uncertainties. For the fake-track background, the vertices can have large displacement, and the fitted vertices have large uncertainties since the tracks are not correlated. For the signals, the fitted vertices would have small uncertainty. For a lighter LLP (hence more boosted), shown in panel (d), the resulting tracks would be more collimated. For a heavier LLP, the resulting tracks spread like two sub-jets, as shown in panel (e).

The distribution of kinetic variables in Eq. 3 are shown in Fig. 5 for the signal, QCD background and fake-track background. For the signal, we show two examples with $m_X = 20$ and 50 GeV, with a lifetime $c\tau_X = 1$ m. To better understand the effect of angular resolution, we show the distribution of variables without the angular smearing effect in Fig. 7 in Appendix VI. In general, since the fake tracks are randomly generated with a large spread in track parameters, we do not expect the angular resolution effect to change fake-track background significantly, which can be clearly seen in Fig. 5 and Fig. 7. Next, we explain the distribution for each variable in detail.

- r_{DV} : the distance between DV and origin in the transverse plane.

The QCD backgrounds jj and $b\bar{b}$ peak around zero, which means the fitted DV locates near the origin in the x - y plane as most of the tracks from QCD are prompt. The distribution of r_{DV} extends up to ~ 0.3 m. Comparing the results with (Fig. 5) and without (Fig. 7) σ_θ , we see that the angular resolution does lead to a broader shape. However, turning off angular resolution does not lead to exact $r_{\text{DV}} = 0$ m. Some charged tracks start from displaced vertices from long lifetime mesons decay, e.g., K_S^0 . There is no significant difference between QCD backgrounds jj and $b\bar{b}$. The reason is that B-meson has a proper lifetime of ~ 0.045 cm, which is too small to generate a difference between jj and $b\bar{b}$.

The fake-track background peaks at around 0.1 m. The related variable from fake-track generation is d_0 , which have a typical value of 0.1 m. The fitted DV is not too far from the reference point for each track, because the reference point is the closest

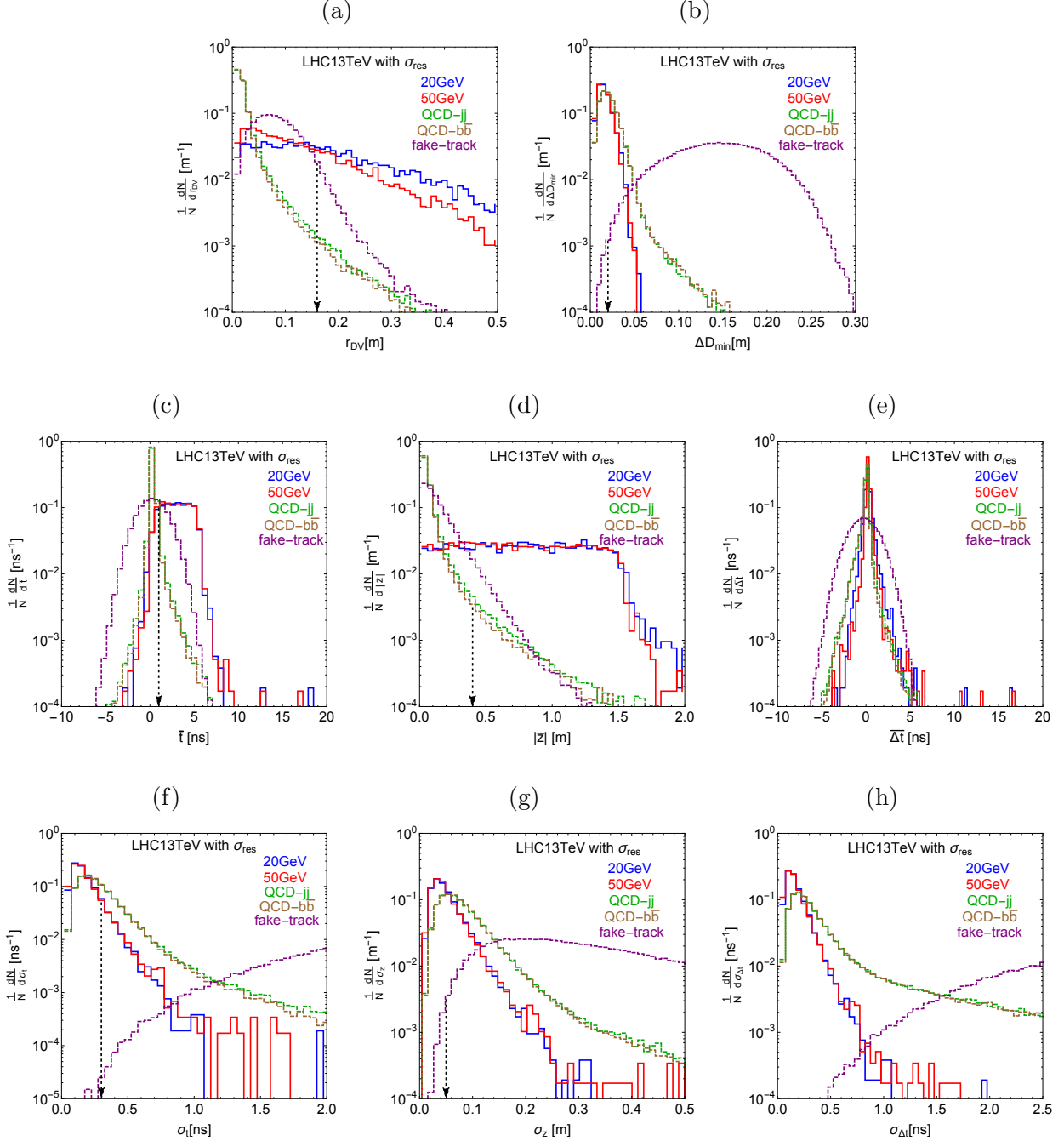


FIG. 5. The kinetic distributions of the leading five tracks for the QCD background, fake-track background and the gluon fusion signal *with* the angular resolution effect applied. The variables are r_{DV} , ΔD_{\min} in the top row, \bar{t} , $|\bar{z}|$, $\overline{\Delta t}$ in the middle, and σ_t , σ_z , $\sigma_{\Delta t}$ in the bottom row. For the signal, we take m_X to be 20 and 50 GeV respectively, with the same lifetime of $c\tau_X = 1$ m. The vertical dotted black line indicates the cut proposed on the variables.

point on the track to the beam spot. This feature can be seen in Fig. 4 (a) as well.

For the signal, r_{DV} is approximately the position where X particle decays in the x - y plane. Its distribution has a very long tail, due to the lifetime of X particle.

- ΔD_{\min} : a measure of how well the set of candidate tracks fit in a common vertex.

Both QCD background and the signal should have a distribution of ΔD_{\min} peaks near zero. As shown in Fig. 5 (b), both of them have a similar shape and a spread of about 0.05 m, mostly from the angular resolution of HGCAL. The size of ΔD_{\min} can be estimated as $\sim \sigma_\theta R \sqrt{5} = 0.03$ m, with $R \simeq 3$ m, and the factor $\sqrt{5}$ comes from the sum of five tracks. This is consistent with Fig. 5 (b). ΔD_{\min} of the fake tracks peaks around 0.2 m, since the tracks have a spread in d_0 of $\mathcal{O}(0.1)$ m and they do not fit well into a common vertex.

Turning off the angular resolution in Fig. 7 (b), the signal events all have exactly $\Delta D_{\min} = 0$ m, which also shows that our algorithm correctly finds the DV where X decays. For the QCD distributions, there are still a few percents of events with non-zero ΔD_{\min} , due to long-lived SM hadrons.

- \bar{t} : the average of the time coordinate of the tracks at the fitted DV.

The QCD background peaks around zero as shown in Fig. 7 (c). The spread of \bar{t} dominantly comes from the angular resolution, and it can be estimated to be $\Delta\phi R/v_T/\sqrt{5}$, where v_T is the transverse velocity of the particle responsible for the track and $\Delta\phi$ is the azimuthal angle change when the track evolved from the fitted DV to the HGCAL. The geometrical acceptance of the HGCAL selects forward tracks, leading to smaller $v_T \sim 0.2 c$, as shown in Fig. 8 in the Appendix. For $\Delta\phi$, its 1σ spread is about 0.02 in Fig. 9 in the Appendix. Therefore, for a typical track radius of $R = 3$ m, the spread of \bar{t} for QCD background is about 0.5 ns, agreeing with Fig. 5.

For the signal, \bar{t} peaks around a few ns, due to the delayed decay of X . In both Fig. 5 and 7, we have chosen $c\tau_X = 1$ m which corresponds to 3 ns. Moreover, decay products from a lighter LLP (hence with a larger boost) has a larger \bar{t} than that of a heavier LLP.

For the fake tracks, the t_i for each track should be determined mainly by the random seed time t_0 , ranging from $\{-6, 6\}$ ns with a flat distribution. The distribution can be

approximated by a Gaussian function peaking around zero, with a standard deviation of $3.5/\sqrt{5} = 1.6$ ns, as shown in Fig. 5 (c). Here 3.5 is an *ad hoc* standard deviation of the flat distribution of each track. In the limit of a large number of tracks, Gaussian function can be used to estimate the spread of the fitted vertex. From Fig. 7 (c), we see that the distribution from the fake-track background is not affected by angular resolution, as expected.

- σ_t : the standard deviation of the time-coordinates of the constituent tracks at the fitted DV.

For the signal and QCD background, the distribution is expected to be concentrated at small values, as shown in Fig. 7. The spread dominantly comes from the angular resolution, as shown in Fig. 5 (f). The spread can be estimated by $\Delta\phi R/v_T$. As explained for \bar{t} , it is ~ 1 ns for QCD background, which agrees with the broad distribution up to a few ns. In addition, some QCD events have large separation between the displaced tracks of the long-lived mesons and the prompt tracks. For the fake-track background, the spread is largely due to the uncorrelated large spread of the track seed time t_0 distributions.

- \bar{z} : the averaged z-coordinate of the tracks at the fitted DV.

We first look at the distribution without σ_θ in Fig. 7. The signals have a very flat distribution because of the long lifetime of X . There is a hard cut because X is required to decay in the region $|z| < 1.5$ m to ensure five stubs for the signal track.

The finite angular resolution σ_θ effects on the distributions of the signal and QCD background are shown in Fig. 5. The signal changes very little because the lifetime and the limited decay region are the dominant factors. The distribution of the QCD background is broadened in a similar fashion as its \bar{t} distribution, the 1σ spread is roughly $0.5\text{ ns} \times v_z \sim 0.15\text{ m}$ with $|v_z| \sim c$ as shown in Fig. 8. The tail in the QCD background extends up to ~ 2 m with less than 10^{-4} probability, in agreement with the \bar{t} distribution which extends to around ~ 8 ns with similar probability. Since $8\text{ ns} \times c \sim 2.4\text{ m}$, this shows a correlation between \bar{t} and \bar{z} . The distribution of the fake-track background follows the exponential shape $e^{-|z|/\sigma}$ with a spread of ~ 0.15 m.

- σ_z : the standard deviation of the z-coordinates of tracks from the fitted DV.

Starting with Fig. 7 without σ_θ , it is exactly zero for the signal and almost zero for QCD background for the similar reason as σ_t . σ_θ broadens the distributions up to 0.15 m for the signal and QCD background, which is in agreement with the previous estimate $(\Delta\phi R/v_T)v_z \sim 0.15$ m. The QCD background has a larger spread than signal, for the same reason as σ_t . For the fake-track background, the large spread in the seed z_0 of the constituent tracks leads to a large spread.

- $\overline{\Delta t}$: the average of the time delay for the tracks.

In Fig. 7, Δt of the signal comes from the slow moving LLP X . Thus, the values of Δt_i are always positive. Moreover, a heavier X moves slower than a lighter X , thus the tail of heavier X is longer than that of the lighter X and the QCD background. The QCD background has a peak around 0 since the track is prompt. The spread around 0 is due to smearing effects and the fact that some tracks come from long-lived meson. The fake-track background distribution is Gaussian-like with 1- σ spread of about 1.5 ns. It is almost symmetric around zero since its 4D parameters are random and independent from each other. The largest spread comes from random t_i , thus $\overline{\Delta t}$ is very similar to \bar{t} .

- $\sigma_{\Delta t}$: the standard deviation of the time delay of the tracks.

Starting with Fig. 7 without σ_θ , the signal has exactly $\sigma_{\Delta t} = 0$, while the QCD background peaks at zero with a spread from long-lived meson decay. The fake background is similar as in σ_t because the dominant spread comes from random t_0 . After including σ_θ , the distributions are broadened as expected but without qualitative change.

We see that the distribution of fake tracks are quite different from signal in general. Based on this, we propose the six cuts according to the distributions and the cut flow table is given in Table V. Explicitly, the cuts for DV fitting variables are,

$$r_{\text{DV}} > 0.16 \text{ m}, \Delta D_{\text{min}} < 0.02 \text{ m}, \bar{t} > 1 \text{ ns}, \sigma_t < 0.3 \text{ ns}, |\bar{z}| > 0.4 \text{ m}, \sigma_z < 0.05 \text{ m}, \quad (4)$$

which we denoted them collectively as *vertexing-cuts*.

B. The transverse impact parameter distribution

The d_0 distributions of the five tracks for the QCD background, fake-track background, and the signal are given in Fig. 6. In Fig. 6 (a), the magnetic field is set as zero, and the angular resolution effect is not included either. The fake tracks have a flat d_0 distribution from its definition. The signal has a broad distribution due to the delayed decay of X . Moreover, the lighter X has a slightly narrower distribution since its decay products are more boosted. The QCD dijet background peaks at $d_0 = 0$ m, with a tail from the long-lived hadron decay.

In Fig. 6 (b), the effect of the magnetic field is included. Comparing with Fig. 6 (a), the QCD background from long-lived hadron are broadened, while the signal is less affected since the displacement before the X decay is more important. The fake-track background is almost flat in d_0 by definition.

Both the magnetic field and the angular resolution effects are included in Fig. 6 (c). Comparing with Fig. 6 (b), the signal is almost unchanged. The QCD background is broadened with a spread of 0.015 m. The spread can be estimated by $\sigma_\theta|z| \sim 0.015$ m, where $|z|$ is taken to be 3.2 m, the distance to HGCAL. The fake-track background is still flat, with its edge smeared by the angular resolution.

In Fig. 6 (d), we have included both the magnetic field and angular resolution effect after applying *vertexing-cuts*. Importantly, the distribution of the QCD background is trimmed to be a Gaussian shape. This is expected since the outliers with large d_0 come from the decay of long-lived hadron, which fails the DV fitting (and thus fail to pass the *vertexing-cuts*). For the signal, the vertex cuts $r_{DV} > 0.16$ m, $\bar{t} > 1$ ns, and $|\bar{z}| > 0.4$ m, selects events in which the X particle decays far from the origin. Any track with small d_0 tracks are significantly affected. The *vertexing-cuts* do not affect the distribution of d_0 of the fake-track background.

C. Correlations between the selection cuts

Due to the limited statistics of our simulation in some cases, we estimate cut efficiencies by the product of the efficiencies of different subsets of cuts. To validate this approach, we study the correlations between those cuts.

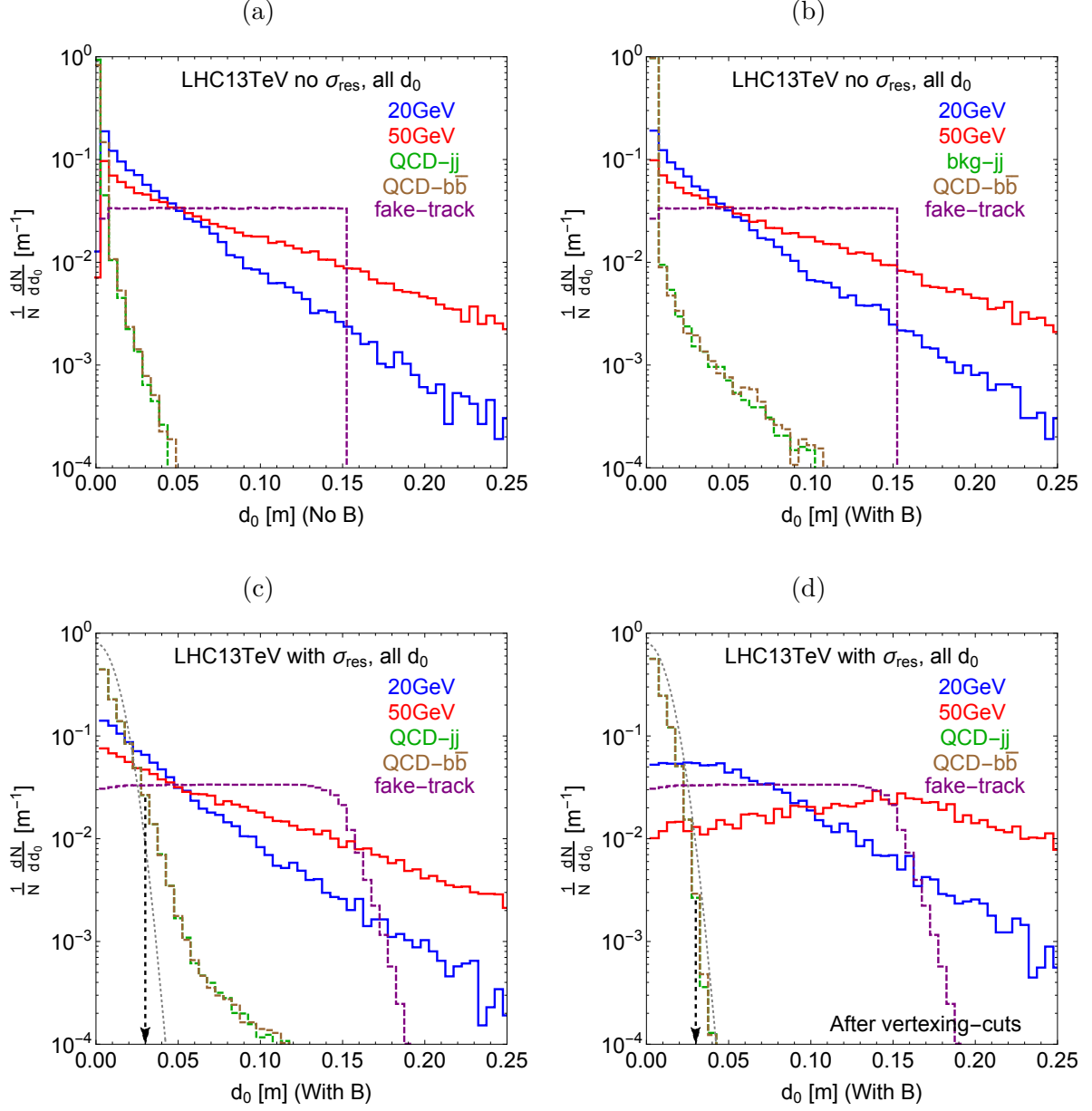


FIG. 6. The distributions of the transverse impact parameter d_0 for the QCD background, the fake-track background and the signal. Panel (a) has no angular resolution effect and no magnetic field. Panel (b) has no angular resolution effect but with a magnetic field of 3.8 Tesla. Panel (c) has the angular resolution effect and the magnetic field. Panel (d) has both effects, and with *vertexing-cuts* imposed. The dotted gray lines are the Gaussian function with a spread of 0.015 m, corresponding to the angular resolution times the z coordinate of the HGICAL.

To quantify the correlations among different cuts, we use the following function

$$\rho_{A,B} \equiv \frac{\epsilon(A)\epsilon(B)}{\epsilon(A\&B)}, \quad (5)$$

where A and B are different cut variables. $\epsilon(A)$ is the efficiency for imposing the corresponding cut A , while $\epsilon(A\&B)$ is the cut efficiency when both A and B cuts are applied. $\rho_{A,B} = 1$ means A and B cuts are *completely independent*. If $\rho_{A,B} \approx \mathcal{O}(1)$, A and B are *approximate independent*. When $\rho_{A,B} \ll 1$, $\epsilon(A)\epsilon(B)$ underestimates $\epsilon(A\&B)$. In this case, using $\epsilon(A)\epsilon(B)$ is *inappropriate* for selection efficiency estimation. For $\rho_{A,B} \gg 1$, $\epsilon(A)\epsilon(B)$ is a *conservative* estimate for background. In summary, if $\rho \gtrsim 1$, using the product of the individual cuts is a reasonable estimate.

jj dijets	$r_{DV} > 0.16$ m (*)	$\Delta D_{\min} < 0.02$ m	$\bar{t} > 1$ ns (*)	$\sigma_t < 0.3$ ns	$ \bar{z} > 0.4$ m (*)	$\sigma_z < 0.05$ m
$(d_0 > 0.01\text{m})^1$	0.70	1.3	0.78	1.1	0.77	1.2
$(d_0 > 0.03\text{m})^1$	0.25	8.6	0.37	1.4	0.40	1.8
$(d_0 > 0.05\text{m})^1$	0.09	35	0.18	2.4	0.19	3.2
$b\bar{b}$ dijets	$r_{DV} > 0.16$ m (*)	$\Delta D_{\min} < 0.02$ m	$\bar{t} > 1$ ns (*)	$\sigma_t < 0.3$ ns	$ \bar{z} > 0.4$ m (*)	$\sigma_z < 0.05$ m
$(d_0 > 0.01\text{m})^1$	0.71	1.3	0.78	1.1	0.77	1.2
$(d_0 > 0.03\text{m})^1$	0.21	8.8	0.36	1.4	0.36	1.8
$(d_0 > 0.05\text{m})^1$	0.07	47	0.16	2.6	0.17	4.0

TABLE I. The correlations $\rho(\text{vertexing-cuts}, d_0)$ for QCD jj and $b\bar{b}$ backgrounds. The columns with (*) are not used to calculate the final selection efficiencies.

We begin with the QCD jj and $b\bar{b}$ backgrounds. First of all, the correlations among *vertexing-cuts* variables are not needed, since we have enough simulated events to compute the efficiency without relying using the product of the efficiencies of the individual cuts. However, the *vertexing-cuts* is not enough to suppress the background; we further require multiple tracks with large d_0 . Here, we are limited by the statistics. Hence, we need to check the the correlation between *vertexing-cuts* and d_0 cuts, and the correlation among different d_0 cuts.

The correlations between *vertexing-cuts* and the d_0 cut are given in Table I. With higher cut threshold of d_0 , the correlation between single d_0 cut and r_{DV} , \bar{t} and $|\bar{z}|$ become stronger. This is expected. For jj and $b\bar{b}$ QCD backgrounds, the event with large transverse impact

parameter is also likely to have large values for r_{DV} , \bar{t} and $|\bar{z}|$. Therefore, we will not use these cuts when calculating the final selection efficiencies. In this way, we avoid double counting and remain *conservative* because all the remaining columns have $\rho > 1$.

jj dijets	$d_0 > 0.01$ m	$d_0 > 0.015$ m	$d_0 > 0.02$ m	$d_0 > 0.025$ m	$d_0 > 0.03$ m
ρ_d^1	0.97 ± 0.016	0.99 ± 0.027	1.0 ± 0.056	1.1 ± 0.15	1.4 ± 0.45
ρ_d^2	1.2 ± 0.04	1.2 ± 0.1	0.69 ± 0.17	-	-
ρ_d^3	1.3 ± 0.11	1.2 ± 0.35	-	-	-
ρ_d^4	1.6 ± 0.30	-	-	-	-
ρ_d^5	1.8 ± 0.83	-	-	-	-
$b\bar{b}$ dijets	$d_0 > 0.01$ m	$d_0 > 0.015$ m	$d_0 > 0.02$ m	$d_0 > 0.025$ m	$d_0 > 0.03$ m
ρ_d^1	1.0 ± 0.017	1.0 ± 0.029	1.0 ± 0.054	1.3 ± 0.17	1.8 ± 0.6
ρ_d^2	1.1 ± 0.041	1.1 ± 0.09	1.0 ± 0.29	-	-
ρ_d^3	1.1 ± 0.087	0.84 ± 0.22	-	-	-
ρ_d^4	1.0 ± 0.15	-	-	-	-
ρ_d^5	0.62 ± 0.16	-	-	-	-

TABLE II. The correlation (including the statistical uncertainty) from our simulation, for multiple d_0 tracks for QCD dijet backgrounds after applying *vertexing-cuts*. For the entries with “-”, there are not enough statistics to make a reliable estimate. For higher tracks multiplicity and d_0 threshold, the results suffer from larger fluctuations due to limited statistics.

Next, we would estimate the cut efficiency on the QCD dijet background by the product of single track efficiency of $d_0 > 0.03$ m. We would like to show that the consecutive d_0 cuts are approximately independent. This is expected since the large d_0 tracks are mainly from detector resolution effects, which are independent between tracks. As shown in Fig. 10 in the Appendix, the d_0 distribution of the leading track is the same as the ensemble of the five tracks shown in Fig. 6. This indicates that we could apply the transverse impact parameter cut on multiple tracks *independently*.⁶ To quantify this further, we define the

⁶ This independence of the tracks is true for both prompt QCD background from smearing effects and for the fake-track background. For the displaced tracks from long-lived hadrons, there is a certain level of correlations which is already removed by our *vertexing-cuts*. Hence, we ignore these minor correlations here.

following function to study the correlations between different d_0 cuts,

$$\rho_d^n \equiv \frac{\epsilon^n(1 \text{ track } d_0 > 0.03\text{m})}{\epsilon(n \text{ tracks } d_0 > 0.03\text{m})}, \quad (6)$$

where $d_0 > 0.03$ m is chosen as an example. Note the tracks in numerator are randomly chosen, while in the denominator they are the n hardest tracks. The correlation ρ_{d_n} for QCD jj and $b\bar{b}$ backgrounds *after* imposing *vertexing-cuts* are given in Table II.

In Table II, from ρ_d^1 to ρ_d^5 , the correlations are mostly around 1, implying the d_0 cuts for different tracks are indeed *independent*⁷. After applying the *vertexing-cuts* and requiring $d_0 > 0.03$ m, we are again limited by the statistics of our simulation. For this reason, ρ_d^1 deviates significantly from 1 here. Similarly, for the entries with “-”, there are not enough statistics to make a reliable estimate. We also check the correlation for multiple d_0 tracks without applying *vertexing-cuts*. The results are shown in Table VI in the Appendix. As expected, they are *approximately independent*.

fake tracks	$r_{\text{DV}} > 0.16$ m	$\Delta D_{\text{min}} < 0.02$ m	$\bar{t} > 1$ ns	$\sigma_t < 0.3$ ns	$ \bar{z} > 0.4$ m	$\sigma_z < 0.05$ m
$r_{\text{DV}} > 0.16$ m		0.47	0.87	0.4	0.16	-
$\Delta D_{\text{min}} < 0.02$ m	0.47		0.95	-	0.51	2.2
$\bar{t} > 1$ ns	0.87	0.95		0.63	0.81	1.1
$\sigma_t < 0.3$ ns	0.4	-	0.63		0.57	-
$ \bar{z} > 0.4$ m	0.16	0.51	0.81	0.57		62
$\sigma_z < 0.05$ m	-	2.2	1.1	-	62	

TABLE III. The correlation table for *vertexing-cuts* variables for the fake-track background. The entries with “-” contain too few events to make a reliable estimate.

Next, we discuss the correlations of the cuts for the fake-track background. Firstly, among the *vertexing-cuts* variables, Table III shows that most of them are *approximately independent*. The correlation between $|\bar{z}|-\sigma_z \gg 1$, which is very *conservative* for an estimate of the background. The correlation between $|\bar{z}|-r_{\text{DV}}$ is 0.16. This is not conservative but it can be compensated by using the $|\bar{z}|-\sigma_z$ pair. Due to low statistics, we do not obtain reliable

⁷ ρ_d^1 is not exactly 1, because the track in the numerator is randomly picked, while the track in the denominator is the leading track. Thus the fact that its value is close to 1 is a kind of proof that different tracks are independent.

estimates for the correlations between $r_{\text{DV}}-\sigma_z$, $\sigma_t-\sigma_z$, and $\sigma_t-\Delta D_{\text{min}}$. As a further check, we evaluated the correlations with a weaker set of cuts thus containing more statistics, shown in Table VII in the Appendix. For example, we relaxed the maximum σ_t cut to 0.5 ns rather than 0.3 ns. In this case, we can conclude the most of the variables are *approximately independent*. In Table VII, the correlations between $r_{\text{DV}}-\sigma_z$, $\sigma_t-\sigma_z$ and $\sigma_t-\Delta D_{\text{min}}$ are 45.4, 0.7 and 2.7 respectively, which are either *approximately independent* or *conservative*. This is consistent with the results in Table III. From these results, we argue that the total cut efficiency for the *vertexing-cuts* variables estimated by using the product of the single cut efficiencies can be considered as conservative.

fake tracks	$r_{\text{DV}} > 0.16 \text{ m}$	$\Delta D_{\text{min}} < 0.02 \text{ m}$	$\bar{t} > 1 \text{ ns}$	$\sigma_t < 0.3 \text{ ns}$	$ \bar{z} > 0.4 \text{ m}$	$\sigma_z < 0.05 \text{ m}$
$(d_0 > 0.01\text{m})^1$	0.97	1.0	1.0	0.94	0.98	1.0
$(d_0 > 0.03\text{m})^1$	0.91	1.1	1.0	1.2	0.94	1.0
$(d_0 > 0.05\text{m})^1$	0.85	1.1	1.0	1.0	0.91	1.1
$(d_0 > 0.03\text{m})^5$	0.65	1.0	0.99	0.76	0.77	1.2

TABLE IV. The correlation between *vertexing-cuts* and d_0 cuts for fake-track background.

We note that there are enough statistics in the fake-track background to calculate the efficiency of the multiple ($d_0 > 0.03\text{m}$) cuts without approximation. Hence, there is no need to check the correlations among individual d_0 cuts here. We are left to check the independence between *vertexing-cuts* and d_0 cuts, which is given in Table. IV. The first three rows show the correlations between the *vertexing-cuts* and various single d_0 cut from 0.01 m to 0.05 m. In the forth row, we use the exact d_0 cuts for five tracks. The result shows the correlations between *vertexing-cuts* and full d_0 cuts are *approximate independent*.

IV. The Results

A. Cut efficiencies

In this section, we present the efficiencies of cuts we adopt in this analysis in Table V. N_{ini} and N_{fin} are the initial and final event numbers before and after imposing the cuts in the table

cut conditions	jj dijet	$b\bar{b}$ dijet	fake-track	ggF $m_s = 20$ GeV	ggF $m_s = 50$ GeV
N_{ini}	5.1×10^{14}	1.1×10^{13}	1×10^{12}	$1.3 \times 10^8 \times \text{BR}$	$1.3 \times 10^8 \times \text{BR}$
5 tracks	8.7×10^{-1}	8.4×10^{-1}	1.0	0.32×0.26	0.72×0.29
$r_{\text{DV}} > 0.16$ m	9.2×10^{-3} (*)	7.5×10^{-3} (*)	4.5×10^{-2}	4.8×10^{-1}	3.1×10^{-1}
$\Delta D_{\text{min}} < 0.02$	6.1×10^{-1}	6.1×10^{-1}	2.2×10^{-3}	8.7×10^{-1}	8.9×10^{-1}
$\bar{t} > 1$ ns	3.3×10^{-2} (*)	2.8×10^{-2} (*)	2.8×10^{-2}	9.9×10^{-1}	9.9×10^{-1}
$\sigma_t < 0.3$ ns	7.1×10^{-1}	7.2×10^{-1}	4.5×10^{-5}	9.6×10^{-1}	9.8×10^{-1}
$ \bar{z} > 0.4$ m	3.4×10^{-2} (*)	2.8×10^{-2} (*)	6.4×10^{-2}	9.9×10^{-1}	9.9×10^{-1}
$\sigma_z < 0.05$	4.9×10^{-1}	4.9×10^{-1}	4.9×10^{-3}	8.5×10^{-1}	8.8×10^{-1}
ϵ_{vtc}	2.1×10^{-1}	2.1×10^{-1}	4.0×10^{-13}	3.4×10^{-1}	2.4×10^{-1}
$(d_0 > 0.03 \text{ m})^5$	$(5.7 \times 10^{-4})^5$	$(6.8 \times 10^{-4})^5$	3.4×10^{-1}	2.6×10^{-1}	8.1×10^{-1}
N_{fin}	5.7×10^{-3}	2.9×10^{-4}	1.4×10^{-1}	$9.7 \times 10^5 \times \text{BR}$	$5.3 \times 10^6 \times \text{BR}$

TABLE V. The cut-flow table for the QCD background, the fake-track background and the signal. N_{ini} and N_{fin} are the initial and final event numbers before and after imposing the cuts. These numbers correspond to an integrated luminosity of $\mathcal{L} = 3 \text{ ab}^{-1}$ at the HL-LHC. “5 tracks” requires each track has $p_T > 1$ GeV and at least 5 tracks arrive at HGICAL. “ ϵ_{vtc} ” is the total efficiency for the *vertexing-cuts* except those with (*). The efficiency of the d_0 cuts is calculated after applying the *vertexing-cuts*. We used the two signal benchmarks with $m_X = 20$ and 50 GeV, and lifetime $c\tau_X = 1$ m.

at the HL-LHC with 13 TeV center-of-mass energy and 3 ab^{-1} integrated luminosity. The row “5 tracks” comes from the requirement that at least five tracks that arrive HGICAL. For the signal, it is the combination of the geometric probability for X decay inside the $|z| < 1.5$ m region and the efficiency for tracks arriving HGICAL. The QCD backgrounds have a better efficiency for tracks arriving HGICAL, because their tracks are more forward than the signal (see the upper panel of Fig. 8). Furthermore, the background jets are usually more energetic thus containing more tracks than the signal, which makes it much easier to satisfy the requirement. The single-cut efficiencies for *vertexing-cuts* DV fitting variables are listed. The variables $\overline{\Delta t}$ and $\sigma_{\Delta t}$ are highly degenerate with \bar{t} and σ_t , and are not used

here⁸. After multiplying N_{ini} by the cut efficiencies in the “5 tracks” row, the “ ϵ_{vtc} ” row and the “ $(d_0 > 0.03\text{m})^5$ ” row, we obtain the final event number N_{fin} .

For the QCD background, we apply a partial set of *vertexing-cuts* on ΔD_{min} , σ_t , and σ_z . The cuts with (*) are correlated with transverse impact parameter d_0 cut. Hence, they are not included in “ ϵ_{vtc} ” to avoid double counting⁹. Furthermore, we apply the single cut efficiency $\epsilon(1 \text{ track } d_0 > 0.03\text{m})$ five times as an estimate of the efficiency requiring all the five tracks with $d_0 > 0.03 \text{ m}$. We found the background the number of the events for jj and $b\bar{b}$ are 5.7×10^{-3} and 2.9×10^{-4} respectively. We have demonstrated that d_0 cuts on different tracks are *approximate independent*, as discussed in detail in the previous section and the appendix. Nevertheless, one might still worry about this is being too aggressive because there is extrapolation in the calculation. We also consider, as an alternative, cutting on only four tracks together with a stronger cut $d_0 > 0.05 \text{ m}$. In this case, the single-cut efficiency for $d_0 > 0.05 \text{ m}$ is about 2.5×10^{-5} for QCD backgrounds. After applying $(d_0 > 0.05 \text{ m})^4$, QCD background can be suppressed down to $\sim 10^{-5}$.

For the fake-track background, we multiply the individual efficiency for each variable in the *vertexing-cuts* and obtain $\epsilon_{\text{vtc}} = 4.0 \times 10^{-13}$. Requiring all five tracks with $d_0 > 0.03 \text{ m}$ can suppress the background further by a factor of 0.34, leaving only 0.14 events. We note that, even though we did not include it in this analysis, the fake-track has to match the track information with the HGCAL calorimeter energy deposit [83], which can further suppress the fake-track background.

In summary, both the QCD background and the fake-track background can be suppressed to be smaller than one event during the lifetime of the HL-LHC. The suppression for the QCD background mainly comes from requiring large track displacement, while displaced vertex reconstruction is mainly responsible for suppressing the fake-track background.

For the signal, the full set of *vertexing-cuts* are applied with a total efficiency of $\epsilon_{\text{vtc}} = 0.34$ and 0.24 for $m_X = 20 \text{ GeV}$ and 50 GeV , respectively. Applying d_0 cuts on all the tracks reduces the signal further. The remaining signal events as a function of branching ratio $\text{BR}(h \rightarrow XX)$ is given in the last row. Heavier X has higher efficiency for several reasons. First, heavier X moves slower, leading to a larger probability of decaying before reaching HGCAL for a fixed proper lifetime. Second, lighter X has only a slightly better efficiency

⁸ For a general discussion on effectiveness of time-delay variable for a broad class of LLP signatures, see Ref. [87].

⁹ One can apply them in an experimental search and it will help to further suppress the QCD background.

under the ϵ_{vtc} cut. Last, lighter X has a lower d_0 cut efficiency, because the tracks tend to be collimated with the direction of X . Therefore, the search is more sensitive to heavier X . For the VBF channel, the distributions of *vertexing-cuts* variables in Fig. 11 and transverse impact parameter d_0 in Fig. 12 are similar to those of the ggF signal. Comparing with the ggF signal, the sensitivity in the VBF channel is weaker by about two orders of magnitude due to the smaller cross-section and the stringent VBF trigger threshold.

B. The reach

The studies in the previous sections prepared us for estimating the reach of new physics with our proposed study. In this section, we present the results for both the ggF channel and the VBF channel. In Fig. 1, we show the projected sensitivity in the Higgs exotic decay into LLPs branching fractions, $BR(h \rightarrow XX)$, as a function of the proper lifetime of the LLP in both the VBF channel and the ggF channel. The VBF search, shown in the left panel, represents a very conservative strategy with the existing VBF trigger. The ggF search, on the right panel, requires a dedicated displaced trigger. The solid line on the bottom of the color shaded region indicates the reach using a 5-displaced-track trigger. While for the solid line on the top of the shaded region, an additional $H_T > 100$ GeV cut is employed. It represents a more conservative version of the displaced trigger, and consequently, it decreases the sensitivity by a factor of 10. The best reach for VBF channel is about $BR(h \rightarrow XX) \sim \mathcal{O}(10^{-4})$, with the LLP lifetime of $c\tau_X \sim 0.1\text{--}1$ meters, while for the ggF channel it is about $BR(h \rightarrow XX) \sim \mathcal{O}(10^{-5}\text{--}10^{-6})$ for a similar lifetime. Alternatively, for an LLP with $c\tau_X \sim 10^3$ meters, the HGCAL based search should be able to probe $BR(h \rightarrow XX)$ down to a few $\times 10^{-4}$ (10^{-2}) in the ggF (VBF) channels, respectively.

For comparison, we show the limits from existing searches for our benchmark signal model in Fig. 1. For very small $c\tau_X$, the best limits come from the ATLAS search for the prompt $h \rightarrow XX \rightarrow 4b$, at 13 TeV with 36.1 fb^{-1} [67]. A short lifetime of X is allowed by the b-tagging algorithm, with maximal sensitivity for $c\tau_X \sim 0.5$ mm. For $c\tau_X$ between $\{10^{-2}, 10^3\}$ m, there are several ATLAS searches using 13 TeV data. One is based on the muon spectrometer (MS) with 36.1 fb^{-1} [18]. The other uses the low- E_T calorimeter energy ratio trigger, with 10.8 fb^{-1} [14]. In the gap for LLP lifetime around cm, the displaced jet searches can be sensitive. A recent CMS search based on displaced vertex in the tracker

system with 139 fb^{-1} obtained limits at the level of 10^{-1} – 10^{-2} [13]. In comparison with these previous searches, our new search shows enhanced sensitivity in the complementary region of the LLP parameter space.

V. Conclusion

High granularity calorimeters offer new opportunities for the search of the long-lived particle. In this work, we study the potential reach for the long-lived particle signal based upon a new search mainly relying on the HGCALE upgrade of the CMS detector. We present results based on both the more conservative traditional VBF trigger and a pair of novel displaced track triggers. Based on a simplified modeling of the signal and background of this new approach, we carefully devised kinematical cuts and estimated the size of the leading backgrounds. HGCALE can obtain the shower direction and timing information with unprecedented precision, enabling us to view them as “tracks”. We find that the QCD background is mostly prompt, which can be suppressed effectively by requiring a large transverse impact parameter for multiple tracks. The second-largest source of background is the fake-track background, which comes from mis-connected hits. The resulting tracks have a random distribution, typically with a large transverse impact parameter. However, it is hard for those tracks to fit in a common vertex. Taking advantage of this feature, we design a set of corresponding *vertexing-cuts* to suppress such backgrounds. The excellent precision of HGCALE in shower direction measurement plays a central role in the effectiveness of these cuts.

Finally, we note here our study is rather conservative in many aspects. For the QCD background and the signal, the most relevant parameter of the HGCALE detector is its angular resolution. In this study, we use the standalone angular resolution from HGCALE. In reality, the track trajectory can be detected by both the tracking system and the tracker inside the HGCALE. Combining the two can further improve the angular resolution. This will result in a better DV fitting and enhance the suppression of the QCD background. Thus, we expect the reach can be further improved. We also require the LLP to decay before reaching the HGCALE detector. With a detailed understanding of the showering behavior of the background, novel searches for LLP decaying *within* the HGCALE can also be sensitive.

This will enable an HGCal standalone trigger, and enlarge the decay volume for the LLP (hence the reach in $c\tau_X$) by a factor of a few.

Acknowledgement

We thank Jared Evans, Yuri Gershtein, Simon Knapen for helpful discussion. JL acknowledges support by an Oehme Fellowship. ZL is supported in part by the NSF under Grant No. PHY1620074 and by the Maryland Center for Fundamental Physics. XPW is supported by the U.S. Department of Energy under Contract No. DE-AC02-06CH11357. LTW is supported by the DOE grant DE-SC0013642. ZL and LTW acknowledge the hospitality of the Kavli Institute for Theoretical Physics, UC Santa Barbara, during the ‘‘Origin of the Vacuum Energy and Electroweak Scales’’ workshop supported by the NSF grant PHY-174958. ZL and LTW would also like to thank Aspen Center for Physics (supported by NSF grant PHY-1607611) for support from their programs and providing the environment for collaboration.

VI. Appendix

We put the supportive figures and tables in the Appendix to avoid redundancy in the main text while keeping helpful information to the readers.

In Fig. 7, kinetic variable distributions for the QCD background, fake-track background and the signal are shown *without* the angular resolution effect included. This is a sanity check for Fig. 5 which *has* included the angular resolution effect. For the distribution of ΔD_{\min} , σ_t , σ_z and $\sigma_{\Delta t}$, the signals are exactly at 0 while the QCD background are peaked at 0. It shows that the DV fitting algorithm has worked well and found the expected true vertex.

In Fig. 8, we plot the distribution of v_T and v_z for the tracks *with* and *without* the requirement to arrive at HGCal. Moreover, we require the track should not hit the barrel electrocalorimeter. In the upper panel, it is clear to see that *without* requiring arriving at HGCal, the $|v_z|$ distribution for all the signal and background have a peak around 1, while a flat valley in the middle. This reflects the distribution of the track zenith angle θ .

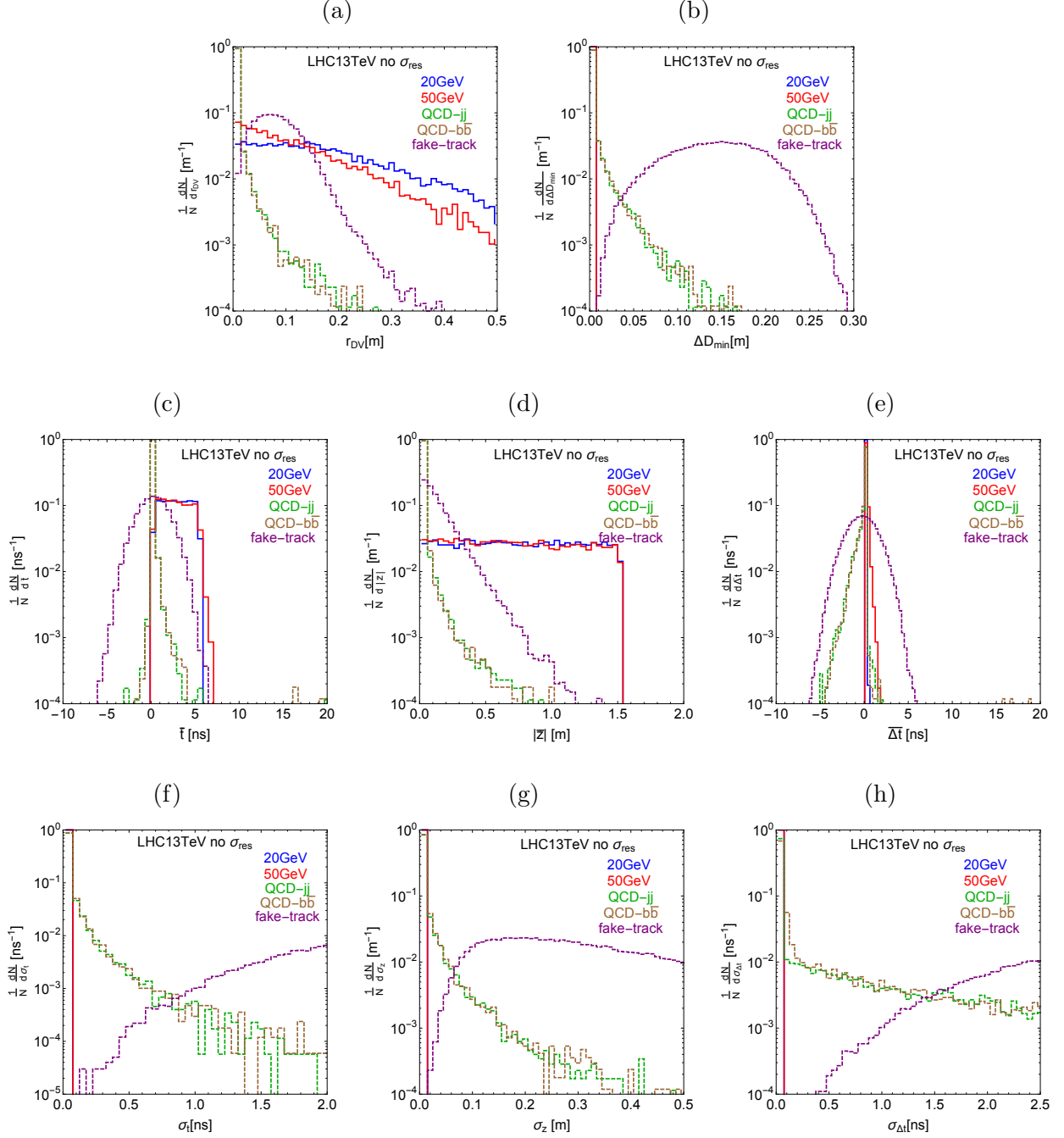


FIG. 7. The kinetic variable distributions for the QCD background, fake-track background and the signal *without* the angular resolution effect included. The variables and definitions are the same as in Fig. 5.

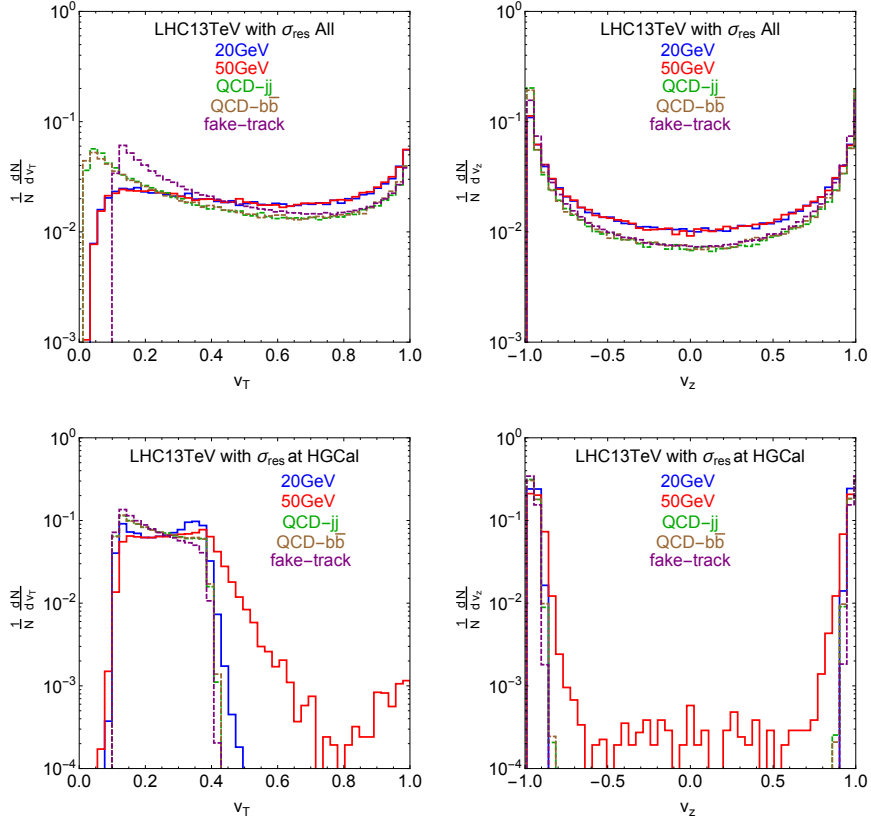


FIG. 8. The distributions of transverse velocity v_T and longitudinal velocity v_z for the tracks *without* (upper panel) and *with* (lower panel) the requirement to arrive at HGCal.

Once requiring arriving at HGCal, we can see that the v_T for signal and backgrounds are dominated by small values, e.g., $0.1 \sim 0.4$. The reason is that HGCal is a forward detector, which picks the forward tracks. Therefore, the v_T is forced to be small.

In Fig. 9, we show the distribution of $\Delta\phi$ for the tracks in the DV fitting procedure. The QCD background and the signal have a similar distribution, peaked with $\Delta\phi = 0$ because they both have a common vertex. $\Delta\phi$ comes from the angular resolution effect of HGCal, which has a spread of about 0.02, which is a few times the angular resolution σ_θ . For fake-track background, the distribution of $\Delta\phi$ has a reason smaller than order 1. From the definition of $\Delta\phi$, its starting point (the reference point) is the closest point to the origin. Hence, the fitted DV should be enclosed within these reference points, as going far from the origin will lead to a bad fit. As a result, the movement in ϕ angle is not large from the starting point to DV.

In Table VI, we show the independence correlation table for multiple d_0 tracks for QCD

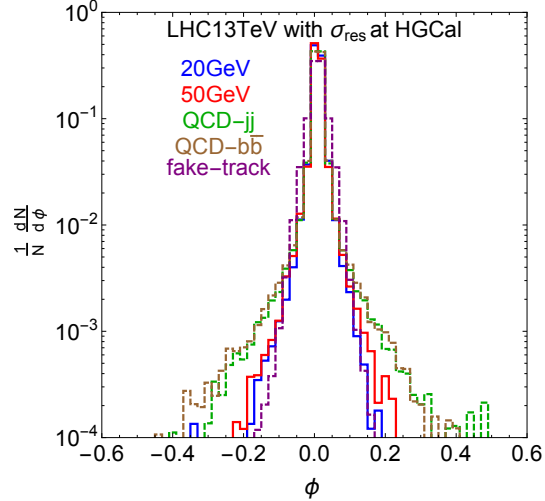


FIG. 9. The distribution of $\Delta\phi$ for the tracks in the DV fitting procedure, where $\Delta\phi$ is the azimuthal angle change when moving from the reference point to the fitted DV.

dijet backgrounds *without* applying *vertexing-cuts*. This is an auxiliary check for Table II. It has higher statistics and also shows the d_0 of different tracks are nicely *independent* under this condition.

The Table VII shows the independence correlation table for *vertexing-cuts* variables for fake-track backgrounds, but with a weaker set of cuts comparing with Table III. We can see that most of the correlations are around 1 (*approximate independent*), with some results are 4.8 and 20 which are *conservative*. With the Table III and Table VII, it indicates that the estimate of fake-track background by multiplying each of these efficiency should be considered as *conservative*.

In Fig. 10, we show the transverse impact parameter d_0 distribution of the leading track for QCD background, fake-track background, and the signal. This figure is similar to Fig. 6, but with only the leading track included.

In Fig. 11 and Fig. 12, the kinetic variables and d_0 distributions for VBF channel are given. One can see that the distributions of the VBF channel are similar to the ggF channel.

jj dijets	$d_0 > 0.01$ m	$d_0 > 0.015$ m	$d_0 > 0.02$ m	$d_0 > 0.025$ m	$d_0 > 0.03$ m
ρ_d^1	1.0 ± 0.06	1.0 ± 0.008	1.0 ± 0.01	1.0 ± 0.015	1.0 ± 0.02
ρ_d^2	1.0 ± 0.01	0.98 ± 0.016	0.96 ± 0.025	0.88 ± 0.038	0.74 ± 0.053
ρ_d^3	0.99 ± 0.018	0.98 ± 0.032	0.90 ± 0.062	0.90 ± 0.15	1.3 ± 0.65
ρ_d^4	0.97 ± 0.027	1.0 ± 0.07	0.75 ± 0.14	-	-
ρ_d^5	0.95 ± 0.04	0.95 ± 0.14	-	-	-
$b\bar{b}$ dijets	$d_0 > 0.01$ m	$d_0 > 0.015$ m	$d_0 > 0.02$ m	$d_0 > 0.025$ m	$d_0 > 0.03$ m
ρ_d^1	1.0 ± 0.06	1.0 ± 0.008	1.0 ± 0.01	1.0 ± 0.015	1.0 ± 0.02
ρ_d^2	1.0 ± 0.01	1.0 ± 0.017	0.97 ± 0.026	0.89 ± 0.40	0.76 ± 0.056
ρ_d^3	0.98 ± 0.018	0.95 ± 0.032	0.93 ± 0.066	0.69 ± 0.1	-
ρ_d^4	0.97 ± 0.027	0.93 ± 0.06	1.1 ± 0.24	-	-
ρ_d^5	0.94 ± 0.04	0.81 ± 0.11	-	-	-

TABLE VI. The correlation table for multiple d_0 tracks for QCD dijet backgrounds *without* applying the *vertexing-cuts*. The symbol “-” means no events left and the number in () indicates the small number of statistics after the cuts. When increasing to multiple tracks and larger d_0 cuts, there are less events thus the result suffers from larger statistic fluctuations. It is an auxiliary check for Table II that is after applying the *vertexing-cuts*.

fake-track	$r_{DV} > 0.05$ m	$\Delta D_{\min} < 0.05$ m	$\bar{t} > 2$ ns	$\sigma_t < 0.5$ ns	$ \bar{z} > 0.4$ m	$\sigma_z < 0.1$ m
$r_{DV} > 0.05$ m		0.82	0.95	1.1	0.75	5.4
$\Delta D_{\min} < 0.05$ m	0.82		0.94	2.7	0.63	2.5
$\bar{t} > 2$ ns	0.95	0.94		0.37	0.54	1.2
$\sigma_t < 0.5$ ns	1.1	2.7	0.37		5.2	0.7
$ \bar{z} > 0.4$ m	0.75	0.63	0.54	5.2		16
$\sigma_z < 0.1$ m	45.4	2.5	1.2	0.7	16	

TABLE VII. The correlation table for *vertexing-cuts* variables for fake-track backgrounds. These cuts are weaker than the cuts in Table III.

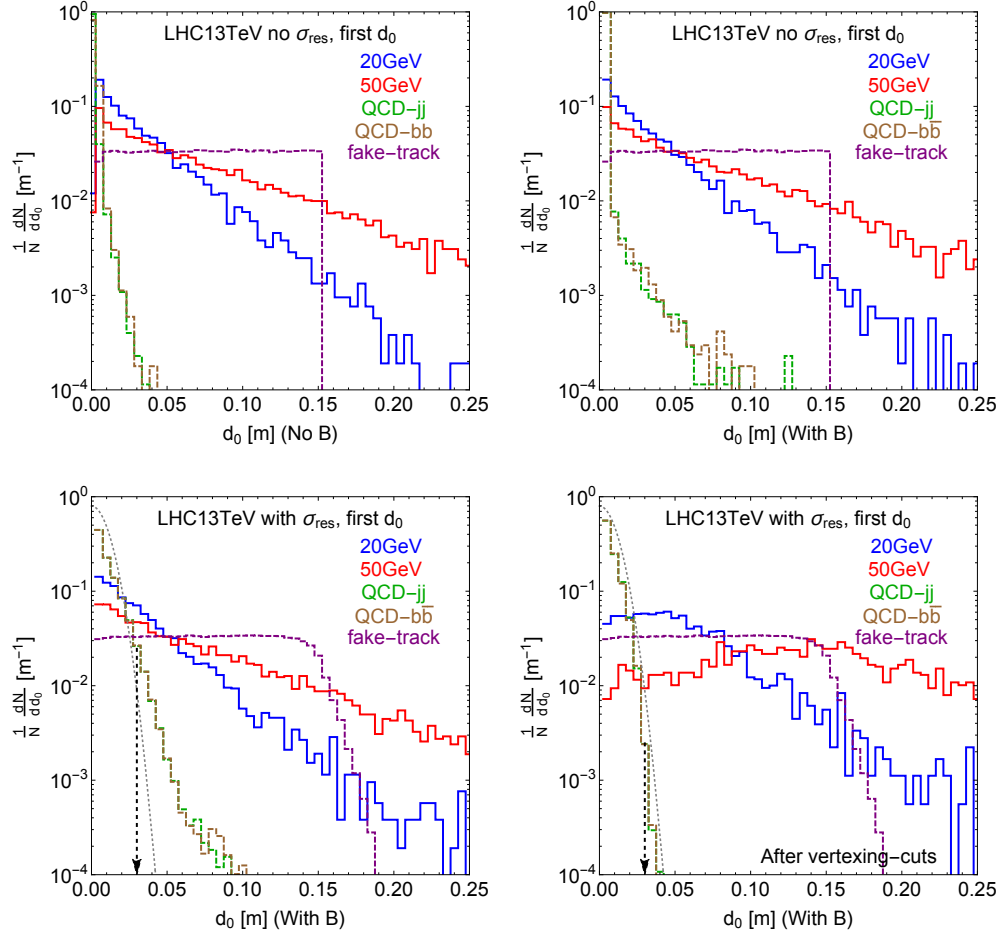


FIG. 10. The transverse impact parameter d_0 distributions for QCD background, fake-track background and the signal. This figure is similar to Fig. 6, but only the leading track distribution is displayed.

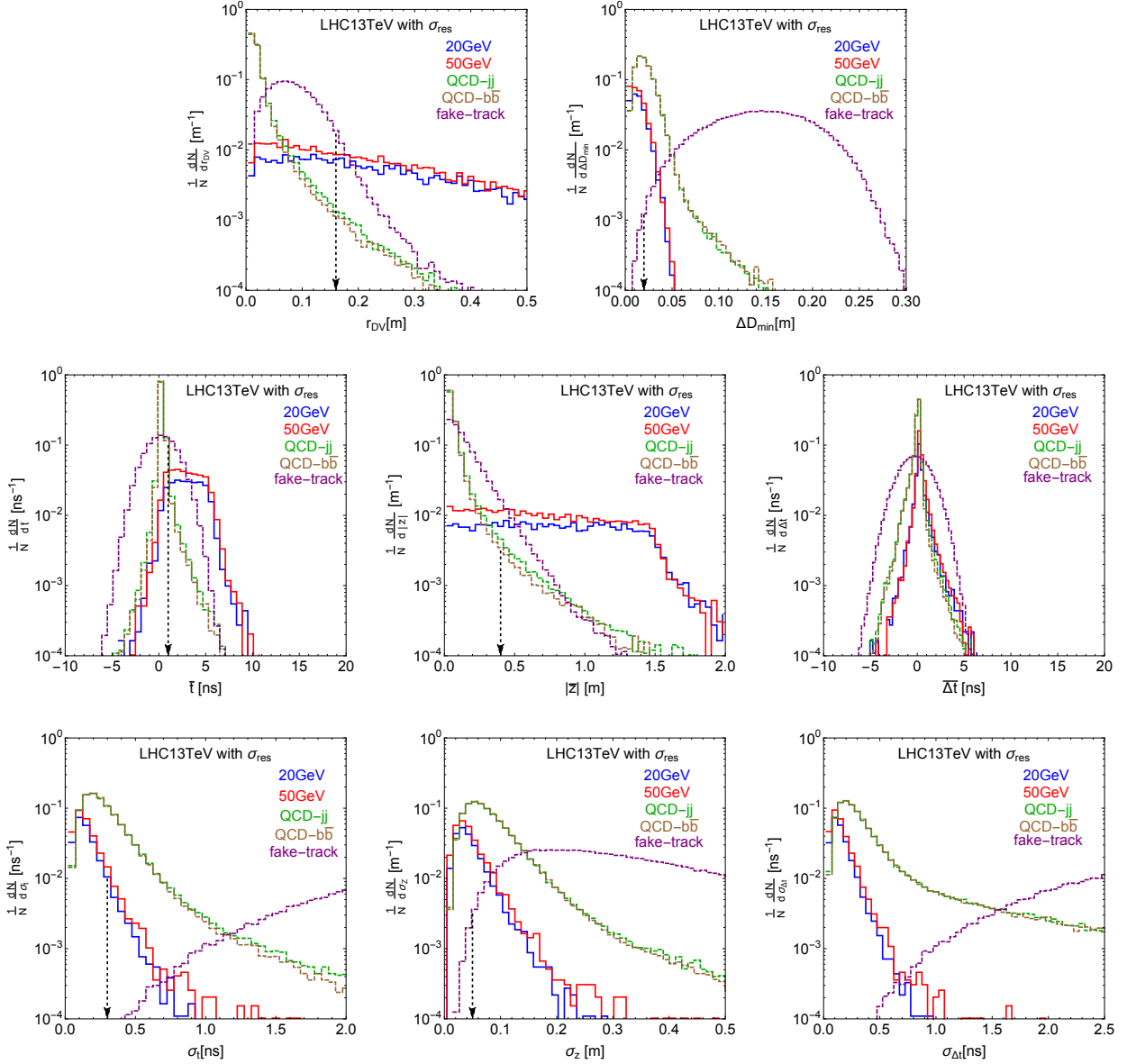


FIG. 11. (VBF channel) The kinetic variable distributions for the QCD background, fake-track background and the signal with angular resolution effect included. The parameter setup is the same as the ggF channel in Fig. 5.

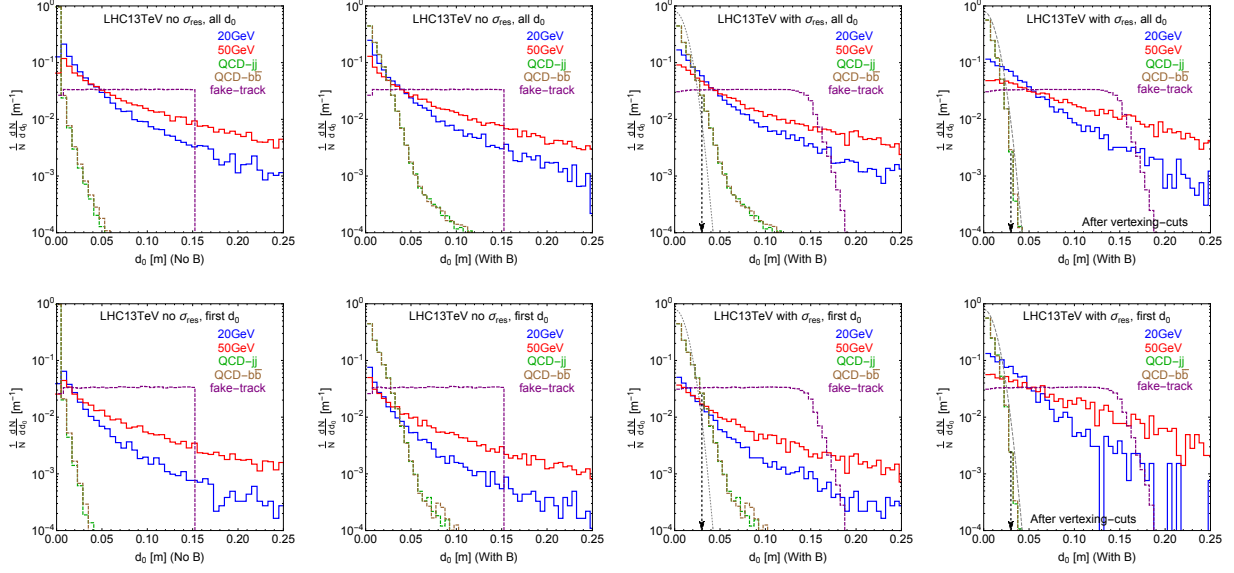


FIG. 12. (VBF channel) The distributions for transverse impact parameter d_0 for QCD background, fake-track background and the signal. The parameter setup is the same as the ggF channel in Fig. 6 and Fig. 10.

-
- [1] J. Alimena *et al.*, “Searching for Long-Lived Particles beyond the Standard Model at the Large Hadron Collider,” [arXiv:1903.04497 \[hep-ex\]](#).
- [2] **ATLAS** Collaboration, G. Aad *et al.*, “Search for nonpointing and delayed photons in the diphoton and missing transverse momentum final state in 8 TeV pp collisions at the LHC using the ATLAS detector,” *Phys. Rev.* **D90** no. 11, (2014) 112005, [arXiv:1409.5542 \[hep-ex\]](#).
- [3] **CMS Collaboration** Collaboration, “Search for long-lived particles using delayed photons with proton-proton collisions at $\sqrt{s} = 13$ TeV,” Tech. Rep. CMS-PAS-EXO-19-005, CERN, Geneva, 2019. <https://cds.cern.ch/record/2682104>.
- [4] **ATLAS** Collaboration, G. Aad *et al.*, “Search for charginos nearly mass degenerate with the lightest neutralino based on a disappearing-track signature in pp collisions at $\sqrt{s}=8$ TeV with the ATLAS detector,” *Phys. Rev.* **D88** no. 11, (2013) 112006, [arXiv:1310.3675 \[hep-ex\]](#).
- [5] **ATLAS** Collaboration, M. Aaboud *et al.*, “Search for long-lived charginos based on a disappearing-track signature in pp collisions at $\sqrt{s} = 13$ TeV with the ATLAS detector,” *JHEP* **06** (2018) 022, [arXiv:1712.02118 \[hep-ex\]](#).
- [6] **CMS** Collaboration, A. M. Sirunyan *et al.*, “Search for disappearing tracks as a signature of new long-lived particles in proton-proton collisions at $\sqrt{s} = 13$ TeV,” *JHEP* **08** (2018) 016, [arXiv:1804.07321 \[hep-ex\]](#).
- [7] **ATLAS** Collaboration, G. Aad *et al.*, “Search for massive, long-lived particles using multitrack displaced vertices or displaced lepton pairs in pp collisions at $\sqrt{s} = 8$ TeV with the ATLAS detector,” *Phys. Rev.* **D92** no. 7, (2015) 072004, [arXiv:1504.05162 \[hep-ex\]](#).
- [8] **ATLAS** Collaboration, M. Aaboud *et al.*, “Search for long-lived, massive particles in events with displaced vertices and missing transverse momentum in $\sqrt{s} = 13$ TeV pp collisions with the ATLAS detector,” *Phys. Rev.* **D97** no. 5, (2018) 052012, [arXiv:1710.04901 \[hep-ex\]](#).
- [9] **CMS** Collaboration, V. Khachatryan *et al.*, “Search for long-lived particles that decay into final states containing two electrons or two muons in proton-proton collisions at $\sqrt{s} = 8$ TeV,” *Phys. Rev.* **D91** no. 5, (2015) 052012, [arXiv:1411.6977 \[hep-ex\]](#).

- [10] **CMS Collaboration**, A. M. Sirunyan *et al.*, “Search for long-lived particles with displaced vertices in multijet events in proton-proton collisions at $\sqrt{s} = 13$ TeV,” *Phys. Rev.* **D98** no. 9, (2018) 092011, [arXiv:1808.03078 \[hep-ex\]](#).
- [11] **CMS Collaboration**, A. M. Sirunyan *et al.*, “Search for long-lived particles decaying into displaced jets in proton-proton collisions at $\sqrt{s} = 13$ TeV,” *Phys. Rev.* **D99** no. 3, (2019) 032011, [arXiv:1811.07991 \[hep-ex\]](#).
- [12] **CMS Collaboration** Collaboration, “Search for displaced leptons in the e-mu channel,” Tech. Rep. CMS-PAS-EXO-16-022, CERN, Geneva, 2016.
<http://cds.cern.ch/record/2205146>.
- [13] **CMS Collaboration** Collaboration, “Search for long-lived particles decaying into displaced jets,” Tech. Rep. CMS-PAS-EXO-19-021, CERN, Geneva, 2020.
<http://cds.cern.ch/record/2717071>.
- [14] **ATLAS Collaboration**, M. Aaboud *et al.*, “Search for long-lived neutral particles in pp collisions at $\sqrt{s} = 13$ TeV that decay into displaced hadronic jets in the ATLAS calorimeter,” *Eur. Phys. J.* **C79** no. 6, (2019) 481, [arXiv:1902.03094 \[hep-ex\]](#).
- [15] **CMS Collaboration**, A. M. Sirunyan *et al.*, “Search for decays of stopped exotic long-lived particles produced in proton-proton collisions at $\sqrt{s} = 13$ TeV,” *JHEP* **05** (2018) 127, [arXiv:1801.00359 \[hep-ex\]](#).
- [16] **ATLAS Collaboration**, G. Aad *et al.*, “Search for long-lived, weakly interacting particles that decay to displaced hadronic jets in proton-proton collisions at $\sqrt{s} = 8$ TeV with the ATLAS detector,” *Phys. Rev.* **D92** no. 1, (2015) 012010, [arXiv:1504.03634 \[hep-ex\]](#).
- [17] **ATLAS Collaboration**, M. Aaboud *et al.*, “Search for long-lived particles in final states with displaced dimuon vertices in pp collisions at $\sqrt{s} = 13$ TeV with the ATLAS detector,” *Phys. Rev.* **D99** no. 1, (2019) 012001, [arXiv:1808.03057 \[hep-ex\]](#).
- [18] **ATLAS Collaboration**, M. Aaboud *et al.*, “Search for long-lived particles produced in pp collisions at $\sqrt{s} = 13$ TeV that decay into displaced hadronic jets in the ATLAS muon spectrometer,” *Phys. Rev.* **D99** no. 5, (2019) 052005, [arXiv:1811.07370 \[hep-ex\]](#).
- [19] J. Heisig and J. Kersten, “Long-lived staus from strong production in a simplified model approach,” *Phys. Rev. D* **86** (2012) 055020, [arXiv:1203.1581 \[hep-ph\]](#).
- [20] K. Barry, P. W. Graham, and S. Rajendran, “Displaced vertices from R -parity violation and baryogenesis,” *Phys. Rev. D* **89** no. 5, (2014) 054003, [arXiv:1310.3853 \[hep-ph\]](#).

- [21] J. C. Helo, M. Hirsch, and S. Kovalenko, “Heavy neutrino searches at the LHC with displaced vertices,” *Phys. Rev. D* **89** (2014) 073005, [arXiv:1312.2900 \[hep-ph\]](#). [Erratum: *Phys.Rev.D* 93, 099902 (2016)].
- [22] Y. Cui and B. Shuve, “Probing Baryogenesis with Displaced Vertices at the LHC,” *JHEP* **02** (2015) 049, [arXiv:1409.6729 \[hep-ph\]](#).
- [23] R. T. Co, F. D’Eramo, L. J. Hall, and D. Pappadopulo, “Freeze-In Dark Matter with Displaced Signatures at Colliders,” *JCAP* **12** (2015) 024, [arXiv:1506.07532 \[hep-ph\]](#).
- [24] Z. Liu and B. Tweedie, “The Fate of Long-Lived Superparticles with Hadronic Decays after LHC Run 1,” *JHEP* **06** (2015) 042, [arXiv:1503.05923 \[hep-ph\]](#).
- [25] J. A. Evans and J. Shelton, “Long-Lived Staus and Displaced Leptons at the LHC,” *JHEP* **04** (2016) 056, [arXiv:1601.01326 \[hep-ph\]](#).
- [26] E. Accomando, L. Delle Rose, S. Moretti, E. Olaiya, and C. H. Shepherd-Themistocleous, “Novel SM-like Higgs decay into displaced heavy neutrino pairs in U(1)’ models,” *JHEP* **04** (2017) 081, [arXiv:1612.05977 \[hep-ph\]](#).
- [27] O. Buchmueller, A. De Roeck, K. Hahn, M. McCullough, P. Schwaller, K. Sung, and T.-T. Yu, “Simplified Models for Displaced Dark Matter Signatures,” *JHEP* **09** (2017) 076, [arXiv:1704.06515 \[hep-ph\]](#).
- [28] R. Mahbubani, P. Schwaller, and J. Zurita, “Closing the window for compressed Dark Sectors with disappearing charged tracks,” *JHEP* **06** (2017) 119, [arXiv:1703.05327 \[hep-ph\]](#). [Erratum: *JHEP* 10, 061 (2017)].
- [29] V. V. Khoze, A. D. Plascencia, and K. Sakurai, “Simplified models of dark matter with a long-lived co-annihilation partner,” *JHEP* **06** (2017) 041, [arXiv:1702.00750 \[hep-ph\]](#).
- [30] A. Ghosh, T. Mondal, and B. Mukhopadhyaya, “Heavy stable charged tracks as signatures of non-thermal dark matter at the LHC : a study in some non-supersymmetric scenarios,” *JHEP* **12** (2017) 136, [arXiv:1706.06815 \[hep-ph\]](#).
- [31] A. Abada, N. Bernal, M. Losada, and X. Marcano, “Inclusive Displaced Vertex Searches for Heavy Neutral Leptons at the LHC,” *JHEP* **01** (2019) 093, [arXiv:1807.10024 \[hep-ph\]](#).
- [32] J. A. Evans and M. A. Luty, “Stopping Quirks at the LHC,” *JHEP* **06** (2019) 090, [arXiv:1811.08903 \[hep-ph\]](#).
- [33] I. Lara, D. E. López-Fogliani, C. Muñoz, N. Nagata, H. Otono, and R. Ruiz De Austri, “Looking for the left sneutrino LSP with displaced-vertex searches,” *Phys. Rev. D* **98** no. 7,

- (2018) 075004, [arXiv:1804.00067 \[hep-ph\]](#).
- [34] M. Nemeṽ sek, F. Nesti, and G. Popara, “Keung-Senjanović process at the LHC: From lepton number violation to displaced vertices to invisible decays,” *Phys. Rev. D* **97** no. 11, (2018) 115018, [arXiv:1801.05813 \[hep-ph\]](#).
- [35] J. C. Helo, M. Hirsch, and Z. S. Wang, “Heavy neutral fermions at the high-luminosity LHC,” *JHEP* **07** (2018) 056, [arXiv:1803.02212 \[hep-ph\]](#).
- [36] G. Cottin, J. C. Helo, and M. Hirsch, “Searches for light sterile neutrinos with multitrack displaced vertices,” *Phys. Rev. D* **97** no. 5, (2018) 055025, [arXiv:1801.02734 \[hep-ph\]](#).
- [37] C. Kilic, S. Najjari, and C. B. Verhaaren, “Discovering the Twin Higgs Boson with Displaced Decays,” *Phys. Rev. D* **99** no. 7, (2019) 075029, [arXiv:1812.08173 \[hep-ph\]](#).
- [38] L. Calibbi, L. Lopez-Honorez, S. Lowette, and A. Mariotti, “Singlet-Doublet Dark Matter Freeze-in: LHC displaced signatures versus cosmology,” *JHEP* **09** (2018) 037, [arXiv:1805.04423 \[hep-ph\]](#).
- [39] M. Drewes and J. Hajer, “Heavy Neutrinos in displaced vertex searches at the LHC and HL-LHC,” *JHEP* **20** (2020) 070, [arXiv:1903.06100 \[hep-ph\]](#).
- [40] M. Du, Z. Liu, and V. Q. Tran, “Enhanced Long-Lived Dark Photon Signals at the LHC,” [arXiv:1912.00422 \[hep-ph\]](#).
- [41] J. Liu, Z. Liu, L.-T. Wang, and X.-P. Wang, “Seeking for sterile neutrinos with displaced leptons at the LHC,” [arXiv:1904.01020 \[hep-ph\]](#). [JHEP07,159(2019)].
- [42] J. Li, T. Li, J. Pei, and W. Zhang, “The quirk trajectory,” [arXiv:2002.07503 \[hep-ph\]](#).
- [43] **SHiP** Collaboration, M. Anelli *et al.*, “A facility to Search for Hidden Particles (SHiP) at the CERN SPS,” [arXiv:1504.04956 \[physics.ins-det\]](#).
- [44] S. Alekhin *et al.*, “A facility to Search for Hidden Particles at the CERN SPS: the SHiP physics case,” *Rept. Prog. Phys.* **79** no. 12, (2016) 124201, [arXiv:1504.04855 \[hep-ph\]](#).
- [45] **LHCb** Collaboration, R. Aaij *et al.*, “Search for Higgs-like bosons decaying into long-lived exotic particles,” *Eur. Phys. J. C* **76** no. 12, (2016) 664, [arXiv:1609.03124 \[hep-ex\]](#).
- [46] A. Coccaro, D. Curtin, H. Lubatti, H. Russell, and J. Shelton, “Data-driven Model-independent Searches for Long-lived Particles at the LHC,” *Phys. Rev. D* **94** no. 11, (2016) 113003, [arXiv:1605.02742 \[hep-ph\]](#).
- [47] S. Antusch, E. Cazzato, and O. Fischer, “Displaced vertex searches for sterile neutrinos at future lepton colliders,” *JHEP* **12** (2016) 007, [arXiv:1604.02420 \[hep-ph\]](#).

- [48] V. V. Gligorov, S. Knapen, M. Papucci, and D. J. Robinson, “Searching for Long-lived Particles: A Compact Detector for Exotics at LHCb,” *Phys. Rev.* **D97** no. 1, (2018) 015023, [arXiv:1708.09395 \[hep-ph\]](#).
- [49] J. L. Feng, I. Galon, F. Kling, and S. Trojanowski, “ForwArd Search ExpeRiment at the LHC,” *Phys. Rev.* **D97** no. 3, (2018) 035001, [arXiv:1708.09389 \[hep-ph\]](#).
- [50] **FASER** Collaboration, A. Ariga *et al.*, “FASER’s physics reach for long-lived particles,” *Phys. Rev.* **D99** no. 9, (2019) 095011, [arXiv:1811.12522 \[hep-ph\]](#).
- [51] D. Curtin, K. R. Dienes, and B. Thomas, “Dynamical Dark Matter, MATHUSLA, and the Lifetime Frontier,” *Phys. Rev. D* **98** no. 11, (2018) 115005, [arXiv:1809.11021 \[hep-ph\]](#).
- [52] D. Curtin *et al.*, “Long-Lived Particles at the Energy Frontier: The MATHUSLA Physics Case,” *Rept. Prog. Phys.* **82** no. 11, (2019) 116201, [arXiv:1806.07396 \[hep-ph\]](#).
- [53] V. V. Gligorov, S. Knapen, B. Nachman, M. Papucci, and D. J. Robinson, “Leveraging the ALICE/L3 cavern for long-lived particle searches,” *Phys. Rev.* **D99** no. 1, (2019) 015023, [arXiv:1810.03636 \[hep-ph\]](#).
- [54] **MATHUSLA** Collaboration, H. Lubatti *et al.*, “MATHUSLA: A Detector Proposal to Explore the Lifetime Frontier at the HL-LHC,” 1, 2019. [arXiv:1901.04040 \[hep-ex\]](#).
- [55] M. Drewes, A. Giammanco, J. Hajer, and M. Lucente, “New long-lived particle searches in heavy-ion collisions at the LHC,” *Phys. Rev.* **D101** no. 5, (2020) 055002, [arXiv:1905.09828 \[hep-ph\]](#).
- [56] G. Aielli *et al.*, “Expression of Interest for the CODEX-b Detector,” [arXiv:1911.00481 \[hep-ex\]](#).
- [57] M. Bauer, O. Brandt, L. Lee, and C. Ohm, “ANUBIS: Proposal to search for long-lived neutral particles in CERN service shafts,” [arXiv:1909.13022 \[physics.ins-det\]](#).
- [58] K. Bondarenko, A. Boyarsky, M. Ovchinnikov, O. Ruchayskiy, and L. Shchutska, “Probing new physics with displaced vertices: muon tracker at CMS,” *Phys. Rev. D* **100** no. 7, (2019) 075015, [arXiv:1903.11918 \[hep-ph\]](#).
- [59] A. Filimonova, R. Schäfer, and S. Westhoff, “Probing dark sectors with long-lived particles at BELLE II,” [arXiv:1911.03490 \[hep-ph\]](#).
- [60] C. Argüelles, P. Coloma, P. Hernández, and V. Muñoz, “Searches for Atmospheric Long-Lived Particles,” *JHEP* **02** (2020) 190, [arXiv:1910.12839 \[hep-ph\]](#).
- [61] K. Cheung and Z. S. Wang, “Probing Long-lived Particles at Higgs Factories,” *Phys. Rev. D*

- 101** no. 3, (2020) 035003, [arXiv:1911.08721 \[hep-ph\]](#).
- [62] C. Yuan, H. Zhang, and Y. Zhao, “Producing and detecting long-lived particles at different experiments at the LHC,” [arXiv:2004.08820 \[hep-ph\]](#).
- [63] B. S. Acharya, A. De Roeck, J. Ellis, D. K. Ghosh, R. Maselek, G. Panizzo, J. L. Pinfold, K. Sakurai, A. Shaa, and A. Wall, “Prospects of searches for long-lived charged particles with MoEDAL,” [arXiv:2004.11305 \[hep-ph\]](#).
- [64] B. Bhattacharjee, S. Mukherjee, R. Sengupta, and P. Solanki, “Triggering long-lived particles in HL-LHC and the challenges in the first stage of the trigger system,” [arXiv:2003.03943 \[hep-ph\]](#).
- [65] B. Shuve and D. Tucker-Smith, “Baryogenesis and Dark Matter from Freeze-In,” [arXiv:2004.00636 \[hep-ph\]](#).
- [66] C. Collaboration, “The Phase-2 Upgrade of the CMS Endcap Calorimeter,” Tech. Rep. CERN-LHCC-2017-023. CMS-TDR-019, CERN, Geneva, Nov, 2017.
<https://cds.cern.ch/record/2293646>. Technical Design Report of the endcap calorimeter for the Phase-2 upgrade of the CMS experiment, in view of the HL-LHC run.
- [67] **ATLAS** Collaboration, M. Aaboud *et al.*, “Search for the Higgs boson produced in association with a vector boson and decaying into two spin-zero particles in the $H \rightarrow aa \rightarrow 4b$ channel in pp collisions at $\sqrt{s} = 13$ TeV with the ATLAS detector,” *JHEP* **10** (2018) 031, [arXiv:1806.07355 \[hep-ex\]](#).
- [68] D. Curtin *et al.*, “Exotic decays of the 125 GeV Higgs boson,” *Phys. Rev. D* **90** no. 7, (2014) 075004, [arXiv:1312.4992 \[hep-ph\]](#).
- [69] M. J. Strassler and K. M. Zurek, “Echoes of a hidden valley at hadron colliders,” *Phys. Lett.* **B651** (2007) 374–379, [arXiv:hep-ph/0604261 \[hep-ph\]](#).
- [70] M. J. Strassler and K. M. Zurek, “Discovering the Higgs through highly-displaced vertices,” *Phys. Lett.* **B661** (2008) 263–267, [arXiv:hep-ph/0605193 \[hep-ph\]](#).
- [71] T. Han, Z. Si, K. M. Zurek, and M. J. Strassler, “Phenomenology of hidden valleys at hadron colliders,” *JHEP* **07** (2008) 008, [arXiv:0712.2041 \[hep-ph\]](#).
- [72] Z. Chacko, H.-S. Goh, and R. Harnik, “The Twin Higgs: Natural electroweak breaking from mirror symmetry,” *Phys. Rev. Lett.* **96** (2006) 231802, [arXiv:hep-ph/0506256 \[hep-ph\]](#).
- [73] Z. Chacko, H.-S. Goh, and R. Harnik, “A Twin Higgs model from left-right symmetry,” *JHEP* **01** (2006) 108, [arXiv:hep-ph/0512088 \[hep-ph\]](#).

- [74] G. Burdman, Z. Chacko, H.-S. Goh, and R. Harnik, “Folded supersymmetry and the LEP paradox,” *JHEP* **02** (2007) 009, [arXiv:hep-ph/0609152 \[hep-ph\]](#).
- [75] N. Craig, A. Katz, M. Strassler, and R. Sundrum, “Naturalness in the Dark at the LHC,” *JHEP* **07** (2015) 105, [arXiv:1501.05310 \[hep-ph\]](#).
- [76] C. Csaki, E. Kuflik, S. Lombardo, and O. Slone, “Searching for displaced Higgs boson decays,” *Phys. Rev. D* **92** no. 7, (2015) 073008, [arXiv:1508.01522 \[hep-ph\]](#).
- [77] D. Curtin and C. B. Verhaaren, “Discovering Uncolored Naturalness in Exotic Higgs Decays,” *JHEP* **12** (2015) 072, [arXiv:1506.06141 \[hep-ph\]](#).
- [78] Y. Gershtein, “CMS Hardware Track Trigger: New Opportunities for Long-Lived Particle Searches at the HL-LHC,” *Phys. Rev. D* **96** no. 3, (2017) 035027, [arXiv:1705.04321 \[hep-ph\]](#).
- [79] J. Alwall, R. Frederix, S. Frixione, V. Hirschi, F. Maltoni, O. Mattelaer, H. S. Shao, T. Stelzer, P. Torrielli, and M. Zaro, “The automated computation of tree-level and next-to-leading order differential cross sections, and their matching to parton shower simulations,” *JHEP* **07** (2014) 079, [arXiv:1405.0301 \[hep-ph\]](#).
- [80] T. Sjostrand, S. Mrenna, and P. Z. Skands, “PYTHIA 6.4 Physics and Manual,” *JHEP* **05** (2006) 026, [arXiv:hep-ph/0603175 \[hep-ph\]](#).
- [81] T. Sjostrand, S. Mrenna, and P. Z. Skands, “A Brief Introduction to PYTHIA 8.1,” *Comput. Phys. Commun.* **178** (2008) 852–867, [arXiv:0710.3820 \[hep-ph\]](#).
- [82] Y. Gershtein and S. Knapen, “A Trigger for Displaced Muon Pairs Following the CMS Phase II Upgrades,” [arXiv:1907.00007 \[hep-ex\]](#).
- [83] A. Hook, S. Kumar, Z. Liu, and R. Sundrum, “The High Quality QCD Axion and the LHC,” [arXiv:1911.12364 \[hep-ph\]](#).
- [84] “Track reconstruction software developments.”
https://indico.cern.ch/event/782953/contributions/3462562/attachments/1888325/3115216/DPF2019_ACTS_Xiaocong.pdf,
https://indico.cern.ch/event/848030/contributions/3601038/attachments/1931352/3198897/WCJ2019_TrackingAndVertexing_VMMCAIRO_22Oct2019.pdf.
- [85] **CMS Collaboration** Collaboration, C. Amendola, “The CMS Level-1 tau lepton and Vector Boson Fusion triggers for the LHC Run II,” Tech. Rep. CMS-CR-2017-346, CERN, Geneva, Oct, 2017. <http://cds.cern.ch/record/2288356>.

- [86] **ATLAS** Collaboration, G. Aad *et al.*, “Search for displaced vertices arising from decays of new heavy particles in 7 TeV pp collisions at ATLAS,” *Phys. Lett. B* **707** (2012) 478–496, [arXiv:1109.2242 \[hep-ex\]](#).
- [87] J. Liu, Z. Liu, and L.-T. Wang, “Enhancing Long-Lived Particles Searches at the LHC with Precision Timing Information,” *Phys. Rev. Lett.* **122** no. 13, (2019) 131801, [arXiv:1805.05957 \[hep-ph\]](#).